2020

# Structure and function of lipid droplet-associated mitochondria in brown adipose tissue

BOSTON UNIVERSITY

SCHOOL OF MEDICINE

Dissertation

# STRUCTURE AND FUNCTION OF LIPID DROPLET-ASSOCIATED MITOCHONDRIA IN BROWN ADIPOSE TISSUE

by

**ILAN YAACOV BENADOR**

B.A., Boston University, 2010

Submitted in partial fulfillment of the

requirements for the degree of

Doctor of Philosophy

2018

Approved by

First Reader

Orian S Shirihai M.D./Ph.D.
Professor of Medicine

Second Reader

Barbara E. Corkey, Ph.D.
Professor of Medicine

## DEDICATION

I would like to dedicate this work to my family. My loving parents Debbie and Marc, my sister Liori, and my fiancée and partner Christine Shen.

## ACKNOWLEDGEMENTS

I would like to thank my mentor Orian Shirihai for his patience, kindness, and extraordinary generosity throughout my graduate experience. Orian's exceptional mentorship helped me develop not only analytical skills and creativity, but also the interpersonal and communication skills essential for effective leadership. I would like to thank everybody in the Shirihai lab who supported and contributed to my time in the lab.

**STRUCTURE AND FUNCTION OF LIPID DROPLET-ASSOCIATED MITOCHONDRIA IN BROWN ADIPOSE TISSUE**

**ILAN YAACOV BENADOR**

Boston University School of Medicine, 2018

Ph.D. degree requirements completed in 2018

Dual M.D./Ph.D. degree expected 2020

Major Professor: Orian Shirihai, M.D., Ph.D., Professor of Medicine

## ABSTRACT

Mitochondria play a central role in lipid metabolism and pathology in obesity and type 2 diabetes mellitus. Mitochondria have been shown to associate with lipid droplets (LDs) in multiple tissues but the functional role of these peridroplet mitochondria (PDM) is unknown. This work reveals that PDM have unique protein composition and cristae structure, and remain adherent to the LD in the tissue homogenate. We developed an approach to isolate PDM based on their adherence to LDs. Comparison of purified PDM to cytoplasmic mitochondria reveals that (1) PDM have increased pyruvate oxidation, electron transport, and ATP synthesis capacities. (2) PDM have reduced beta oxidation capacity and depart from LDs upon activation of brown adipose tissue thermogenesis and beta oxidation. (3) PDM support LD expansion as Perilipin 5-induced recruitment of mitochondria to LDs increases ATP-dependent triacylglyceride synthesis. (4) PDM maintain a

distinct protein composition due to uniquely low fusion-fission dynamics. We conclude that PDM represent a segregated mitochondrial population with unique structure and function that supports triacylglyceride synthesis. We suggest that increased mitochondrial recruitment to LDs may be part of a generalized adaptive response in physiological conditions that require LD expansion, such as post-prandial lipid synthesis and storage. Furthermore, PDM-mediated LD expansion may play a role in muscle and liver injury from lipotoxicity in conditions of nutrient excess, such as obesity and hyperlipidemia. A better understanding of PDM and LD biology may therefore lead to new therapies for lipotoxic tissue injury and insulin resistance.

*A good case can be made of our nonexistence as entities. We are not made up, as we had always supposed, of successively enriched packets of our own parts. We are shared, rented, occupied. At the interior of our cells, driving them, providing the oxidative energy that sends us out for the improvement of each shining day, are the mitochondria, and in a strict sense they are not ours. They turn out to be little separate creatures, the colonial posterity of migrant prokaryotes, probably primitive bacteria that swam into ancestral precursors of our eukaryotic cells and stayed there. Ever since, they have maintained themselves and their ways, replicating in their own fashion, privately, with their own DNA and RNA quite different than outs. Mitochondria are stable and responsible lodgers, and I choose to trust them. Without them, we would not move a muscle, drum a finger, think a thought.*

*-Lewis Thomas*

## TABLE OF CONTENTS

## LIST OF TABLES

## LIST OF FIGURES

## LIST OF ABBREVIATIONS

ATP ..... adenosine triphosphate

BAT ..... brown adipose tissue

BODIPY ..... boron dipyrromethene 493/503

C12 ..... boron dipyrromethene C12 558/568

CS ..... citrate synthase

CM ..... cytoplasmic mitochondria

CoA ..... coenzyme a

COX ..... cytochrome oxidase

DGAT .....diacylglycerol acyltransferase

DRP1DN.....DRP1 dominant negative

DTNB..... 5′-Dithiobis(2-nitrobenzoic acid)

EM ..... electron microscopy

FI .....fluorescence intensity

GDP..... guanosine diphosphate

KRB .....krebs ringer bicarbonate buffer

LD.....lipid droplet

MAS..... mitochondrial assay solution

Mfn .....mitofusin

mLD..... micro lipid droplet

MMP ..... mitochondrial membrane potential

mtDsRed .....mitochondrially targeted red fluorescence protein

mtPAGFP ..mitochondrially targeted photo activatable green fluorescence protein

NAD(P)H ..... nadh and nadph

OCR ..... oxygen consumption rate

OXPHOS .....oxidative phosphorylation

Plin .....perilipin

SHE .....sucrose hepes egta

TAG .....triacylglyceride

TLC.....thin layer chromatogrpahy

TMRE ..... tetramethylrhodamine ethyl ester perchlorate

UCP1 ..... uncoupling protein 1

# CHAPTER ONE: General Introduction

## The obesity epidemic

Obesity is a rapidly rising epidemic that is associated with significant morbidity and mortality (Mitchell, Catenacci, Wyatt, & Hill, 2018). Obesity, defined as body mass index > 30kg/$m^2$, currently affects one in three U.S. adults and disproportionally African and Hispanic Americans. Obese individuals have dramatically increased risk for developing type 2 diabetes mellitus, cardiovascular disease, cancer, and early death. In addition to the health consequences of obesity and type 2 diabetes, these diseases are associated with over $407.6 billion in direct costs and lost productivity. Improving the prevention and treatment of obesity is therefore of paramount importance for our collective health and prosperity.

## Obesity pathology and treatment

Obesity is characterized by increased levels of circulating lipids that cause direct and indirect damage to most of the body's major organ systems and vascular networks (Klop, Elte, & Cabezas, 2013). In healthy individuals, ingested foodstuffs are oxidized after a meal or sequestered into storage in the form of glycogen and triacylglycerides. During periods of fasting, the stored nutrients are released to maintain a constant nutrient supply to vital body organs. The alternate ingestion of foodstuffs and release of stored nutrients maintains a constant healthy level of circulating nutrients (~70-120mg/dL glucose and 50-150 mg/dL triacylglycerides). However, in obese individuals, excessive food intake combined with increased

endogenous glucose and lipid release results in chronically elevated levels of circulating nutrients, leading to gluco- and lipo- toxicities. Excess glucose and lipids accumulate in blood vessel walls, leading to microvascular injuries (nephropathy, peripheral neurophathy, retinopathy) in addition to promoting further insulin resistance and metabolic dysfunction. Prolonged exposure to high nutrients results in increased risk for macrovascular injuries (heart attack and stroke), ectopic fat deposition (non-alcoholic fatty liver disease and cardiomyopathy), and increased mortality.

Efficacious treatment for obesity is currently severely limited. Diet, exercise, and lifestyle modifications are the primary methods of treatments but have limited long-term success. Drug therapies include compounds that directly inhibit nutrient absorption from the gut or curb appetite by acting on satiety receptors in the central nervous system. For qualified patients, surgical resection of the gastrointestinal system is used as a last measure to limit nutrient intake and absorption when other approaches fail. Thus, there is a dire need to identify new and better ways to prevent and treat obesity.

**Brown adipose tissue**

Much of the treatment of obesity has thus far focused on weight loss and specifically the reduction of adipose tissue. However, not all adipose tissue is the same. While white adipocytes specialize in storing fatty acids and subsequently releasing them for other tissues to consume, brown adipocytes utilize lipid stores

for thermogenic fat oxidation in cold exposure (Barbara Cannon & Nedergaard, 2004). Brown adipose tissue thermogenesis occurs due to the unique expression of Uncoupling protein 1 (UCP1), which permits increased rates of fatty acid consumption by uncoupling nutrient oxidation from ATP synthesis. Brown adipose tissue is therefore viewed as a therapeutic approach to reduce excess circulating fatty acids in and enhance weight loss in obese individuals (Boss & Farmer, 2012).

**Intracellular fat metabolism**

Mitochondria are the primary site of fatty acid oxidation in mammalian cells (Eaton, 2002). Fatty acids are an essential fuel because of their high energy density and storage capacity relative to glucose. Indeed, mammals rely almost exclusively on fatty acids when fasting for more than several hours as well as during prolonged exercise when glycogen stores are depleted. Most cells store fatty acids as triacylglycerides in the form of lipid droplets to prevent toxicity from high levels of free fatty acids. Fatty acid packaging into triacylglycerides is an energy demanding process involving ATP-dependent ligation to coenzyme A followed by sequential esterification reactions to a glycerol backbone. While lipid droplets were initially viewed as static storage compartments for triacylglycerides, research from the last decade has revealed that lipid droplets have a distinct proteome with dynamic signaling networks (Farese & Walther, 2009). For example, when fatty acids are needed to fuel the cell, multiple signaling pathways recruit and activate lipase enzymes at the surface of lipid droplets (Zechner et al., 2012). Once liberated from

the lipid droplet, fatty acids are again ligated to coenzyme A in order to be processed for mitochondrial oxidation. The mitochondrial outer membrane protein CPT1 converts fatty acyl-coas to acyl-carnitines (Eaton, 2002), which are then shuttled into the mitochondrial matrix through the voltage-dependent anion channel and the inner membrane carnitine-acylcarnitine translocase. Once inside the matrix, fatty acyl-carnitines are converted back to acyl-coas by CPT2 and finally oxidized to produce NADH, FADH2, and acetyl-coA in a process called beta-oxidation. While CPT1 has been shown to play a key role in regulating fat oxidation in liver and muscle tissue, the precise mechanisms by which mitochondria dynamically switch between glucose to fatty acid oxidation are still unclear. A better understanding of fat metabolism is therefore essential to improve obesity treatment.

# CHAPTER TWO: Mitochondria Bound to Lipid Droplets Have Unique Bioenergetics, Composition, and Dynamics That Support Lipid Droplet Expansion


## Abstract

Mitochondria associate with lipid droplets (LDs) in fat-oxidizing tissues but the functional role of these peridroplet mitochondria (PDM) is unknown. Microscopic observation of interscapular brown adipose tissue reveals that PDM have unique protein composition and cristae structure, and remain adherent to the LD in the tissue homogenate. We developed an approach to isolate PDM based on their adherence to LDs. Comparison of purified PDM to cytoplasmic mitochondria reveals that (1) PDM have increased pyruvate oxidation, electron transport, and ATP synthesis capacities. (2) PDM have reduced beta oxidation capacity and depart from LDs upon tissue activation of thermogenesis and beta oxidation. (3) PDM support LD expansion as Perilipin 5-induced recruitment of mitochondria to LDs increases ATP-dependent triacylglyceride synthesis. (4) PDM maintain a distinct protein composition due to uniquely low fusion-fission dynamics. We conclude that PDM represent a segregated mitochondrial population with unique structure and function that supports triacylglyceride synthesis.


## Introduction

Studies have shown that mitochondria contact lipid droplets (LDs) in tissues with high fatty acid storage and oxidation capacity, including brown adipose tissue

(Boutant et al., 2017), heart (H. Wang et al., 2013), and Type I skeletal muscle (Tarnopolsky et al., 2007). Furthermore, mitochondria-LD association was shown to be highly regulated by Perilipin5 (Plin5), a LD coat protein highly expressed in fat-oxidizing tissues (H. Wang et al., 2011). The high degree of regulation and tissue-specificity support the concept that peridroplet mitochondria (PDM) play a specialized role in fat metabolism. However, it remains unclear whether PDM promote lipid oxidation (Rambold, Cohen, & Lippincott-Schwartz, 2015), lipid storage (Nguyen et al., 2017; Stone et al., 2009; H. Wang et al., 2011), or both.

In this study, we sought to determine the role of PDM in a system where a robust shift can occur between fat storage and oxidation. Brown adipose tissue (BAT) acutely turns on uncoupled lipid oxidation upon adrenergic stimulation (Barbara Cannon & Nedergaard, 2004). Functional specialization and segregation of mitochondrial subpopulations may allow BAT mitochondria to perform the contradictory tasks of uncoupled fatty acid oxidation and ATP generation for fatty acid activation by Coenzyme A (CoA) addition. However, it remains unclear whether functional specialization and segregation is possible in brown adipocytes where fusion and fission continuously equilibrate the content across the mitochondrial population within each adipocyte (Wikstrom et al., 2014). Furthermore, there are currently no established methods to isolate PDM, leaving their function, composition, and bioenergetics unknown.

In this study, we developed an approach to isolate PDM from BAT based on their adherence to LDs. Our results demonstrate that PDM represent a segregated mitochondrial subpopulation with distinct composition, bioenergetics, and dynamics that support triacylglyceride synthesis.

## Results

### Isolation of peridroplet mitochondria by differential centrifugation

Little is currently known about peridroplet mitochondria (PDM) due to the lack of reliable methods to selectively isolate PDM. The tight association between mitochondria and lipid droplets (LDs) observed in electron micrographs (EMs)(Wikstrom et al., 2014) and in biochemical studies (Yu et al., 2015) led us to hypothesize that mitochondria-LD association could withstand mechanical cell disruption. To test this, we disrupted interscapular brown adipose tissue (BAT) using a dounce homogenizer, separated the fat layer by low-speed centrifugation, and co-stained it with the neutral lipid dye BODIPY 493/503 (BODIPY) and the mitochondrial dye MitoTracker deep red (MitoTracker)(Figure 2.1A). Super-resolution confocal microscopy revealed numerous LDs surrounded by tubular MitoTracker-stained structures, suggesting that mitochondria-LD association was preserved in the fat layer (Figure 2.1B). Next, to separate PDM from LDs, we centrifuged the fat layer at high speed, a procedure previously shown to strip LD proteins (Ding et al., 2013). The stripped fat layer contained over 50% fewer LDs

with MitoTracker fluorescence (Figures 2.1C-D), suggesting that LDs were effectively stripped of PDM. The resulting peridroplet mitochondrial (PDM) pellet contained MitoTracker-positive particles and little to no BODIPY staining (Figure 2.1E), suggesting that PDM were successfully separated from LDs. To confirm that PDM were not contaminated with LD remnants, we quantified the LD content under low magnification microscopy (Figure 2.1F-G). Low-magnification images revealed that PDM pellet had over 95% lower LD content compared to the fat layer (Figure 2.1G). Furthermore, the level of LD contamination within the PDM pellet was similar to the LD contamination within the cytoplasmic mitochondria (CM) pellet isolated from the supernatant (Figures 2.1A, 2.1G). These results suggest that LDs were effectively removed from PDM by differential centrifugation.

Since differential centrifugation results in relatively crude preparations, we next determined the mitochondrial protein content in CM and PDM fractions by mass spectrometry. Protein annotation using MitoCarta2.0 (Calvo, Clauser, & Mootha, 2016) revealed that 5969 out of 10935 (54.5%) identified peptides belonged to mitochondrial proteins in PDM compared to 5979 out of 11812 (50.6%) in CM (Figure 2.1H). Furthermore, analysis of previously published BAT mitochondria proteomics data revealed a 46.9% enrichment of mitochondrial protein (Forner et al., 2009). These results suggest that mitochondrial protein enrichment in CM and PDM fractions were comparable and within the range of previously published methods.

Next, to determine whether CM and PDM preparations can generate a similar membrane potential, we stained the preparations with the membrane potential-sensitive rosamine dye MitoTracker Red. To control for mitochondrial mass, we co-stained preparations with the mitochondrial protein dye MitoTracker Green (Cottet-Rousselle, Ronot, Leverve, & Mayol, 2011). Fluorescence microscopy revealed no significant differences in the MitoTracker Red-to-Green fluorescence ratio between CM and PDM (Figures 2.1I-J), suggesting that CM and PDM preparations were equally capable of generating a membrane potential.

**Peridroplet mitochondria have increased respiratory capacity**

To characterize the respiratory capacity of PDM, we measured their oxygen consumption rate using Seahorse XF96 extracellular flux analyzer. Isolated PDM and CM were loaded into different wells of the same seahorse plate and assayed with pyruvate and malate as fuels. Prior to the assay, we confirmed that equal levels of mitochondrial protein and functional mitochondria were present in CM and PDM preparations by mass spectrometry analysis (Figure 2.1H) and membrane potential imaging (Figures 2.1I-J), respectively. Furthermore, we confirmed equal mitochondrial mass was loaded into the XF96 flux analyzer plate by directly staining and imaging the wells with MitoTracker (Figures 2.2A-B).

PDM assayed using pyruvate and malate as fuels showed a 2-fold increase in both ATP-synthesizing respiration (State III) and maximal respiratory capacity induced by uncoupling with FCCP (Maximal) when compared to CM (Figures 2.2C-E).

Enhanced ATP synthesis and maximal electron transport capacities in PDM were not limited to pyruvate oxidation since a similar increase was observed when assayed with the fuel succinate (Figure 2.1S).

To determine whether increased PDM respiratory capacity is associated with higher capacity of respiratory enzyme complexes, we next assessed the activity of individual complexes in isolated mitochondria. Cytochrome c oxidase (COX) activity was determined by measuring oxygen consumption rate using TMPD/ascorbate. We injected Antimycin and rotenone at the start of the assay and the COX-specific inhibitor sodium azide at the end of the assay to confirm that TMPD/ascorbate-driven respiration was specific to COX activity. TMPD/ascorbate-driven respiration was 68±27.5% higher in PDM compared to CM (Figures 2.2F-G), confirming that isolated PDM have higher COX activity compared to CM.

Next, we determined ATP synthase function in isolated mitochondria using firefly luciferase luminescence. We determined the optimal concentration of reagents and photometric measurement settings using HPLC-purified ATP standards and controlled for non-OXPHOS ATP synthesis using the ATP synthase inhibitor oligomycin. PDM had 210.4±62.8% higher rate of luminescence increase compared to CM (Figures 2.2H-I), confirming isolated PDM have higher ATP synthesis capacity compared to CM.

Next, to determine whether higher respiratory capacity observed in isolated PDM can be detected in living cells, we assessed mitochondrial membrane potential

using the reversible membrane potential-sensitive dye tetramethylrhodamine-ethyl-ester-perchlorate (TMRE). TMRE fluorescence intensity was not significantly different between CM and PDM at baseline, suggesting that increased PDM proton pumping by electron transport complexes may be matched by higher proton flux through ATP synthase. If this were the case, we reasoned that blocking ATP synthase will cause an acute hyperpolarization of PDM as compared to CM. Indeed, oligomycin treatment revealed PDM with higher TMRE fluorescence intensity compared to CM (Figures 2.2J-K), suggesting that PDM have higher proton efflux rate compared to CM. Taken together, these results suggest that PDM have enhanced oxidative phosphorylation capacity.

**Peridroplet mitochondria have increased levels of cytochrome c oxidase, ATP synthase, and super complex I+III assembly.**

We reasoned that increased electron transport and ATP synthesis capacities in PDM could result from increased expression levels of protein associated with oxidative phosphorylation. To test this, we assessed levels of each OXPHOS complex by Western blot analysis of complex subunits. We confirmed equal amounts of protein were loaded by staining Western blot membranes with the non-specific protein dye Ponceau S (Figure 2.3A). To control for mitochondrial protein loading, bands were normalized to the mitochondrial marker TOM20, which did not vary significantly between samples (Figure 2.2S).

Western blot analysis revealed that PDM have 15.6±4.5% higher levels of cytochrome c oxidase subunit 4 (COX4) protein and 8.7±4.8% higher ATP Synthase subunit α (ATP5a1) protein relative to CM (Figures 2.3B-C). We confirmed that detected differences were independent of loading and band saturation by performing a dilution blot and histogram analysis, respectively (Figures 2.2). We observed no significant differences in Complex I, Complex II, nor Complex III subunit levels (Figures 2.2B-C). Given the relatively small differences in complex protein levels, we rationalized that enhanced PDM respiratory capacity could be due to increased assembly of respiratory super complexes (Lapuente-Brun et al., 2013; Rosca et al., 2008). To test this, we measured super-complex assembly by blue native PAGE. Remarkably, Blue native PAGE revealed 29.5±8.2% higher levels of Complex I + Complex III super-assembly in PDM relative to CM (Figures 2.3D-E). These results suggest that specialized OXPHOS protein composition and super assembly may contribute to enhanced PDM respiratory capacity.

**High levels of cytochrome c oxidase and ATP synthase are preferentially localized to PDM**

To determine the relative levels of OXPHOS proteins in CM and PDM within intact brown adipocytes we next measured protein levels by immunofluorescence. We confirmed antibody specificity by probing a whole Western blot membrane with each individual antibody and exclusively detecting a single band corresponding to

the protein of interest (Figure 2.2S). Super-resolution confocal imaging of immunostained cells revealed heterogeneous distribution of OXPHOS protein in PDM and CM populations (Figures 2.3F-I). Subcellular distribution analysis revealed that mitochondria with the highest levels of COX4 and ATP synthase α are exclusively PDM. Remarkably, some LDs were surrounded by ATP synthase-rich PDM, while other LDs within the same cell were surrounded by PDMs with lower ATP synthase levels comparable to CM. This remarkable heterogeneity may explain the relatively small changes we detected by Western blot analysis of the average protein expression of isolated CM and PDM.

**Peridroplet mitochondria have lower fatty acid oxidation capacity but increased TCA cycle capacity**

Our results show that PDM have enhanced OXPHOS protein levels and respiratory capacity. However, these results were not sufficient to determine whether PDM have a preference for fuel oxidation by beta oxidation or through the TCA cycle. If PDM are specialized for fat oxidation, we reasoned that 1. isolated PDM will have enhanced fatty acid oxidation capacity, 2. PDM will have enhanced levels of uncoupling protein 1 (UCP1), and 3. mitochondrial contact with LDs will be increased during cold-induced thermogenesis, when fatty acid oxidation rate is maximal.

To test these predictions, we measured fatty acid-driven respiration and UCP1 content in isolated mitochondria. Contrary to our prediction, maximal respiration

driven by palmitoyl-carnitine was significantly lower in PDM compared to CM (Figures 2.4A-B). We confirmed that PDM have reduced fatty acid oxidation capacity by normalizing fat oxidation capacity to pyruvate oxidation capacity assayed in parallel wells on the same seahorse XF96 plate (Figure 2.3S). Furthermore, Western blot analysis showed no difference in UCP1 levels (Figure 2.4C), suggesting that PDM are not specialized for thermogenic fat oxidation.

Since mitochondrial beta oxidation and TCA flux are two competing pathways (Garland, Shepherd, Nicholls, & Ontko, 1968), we next tested whether enhanced PDM respiratory capacity is supported by higher capacity for TCA cycling. To this end, we determined the activity of the TCA enzyme citrate synthase (CS) by 5,5′-dithio-bis(2-nitrobenzoic acid) (DTNB) absorbance assay. DTNB reduction rate was 33.1±9.7% higher in isolated PDM compared to CM (Figures 2.4D-E), suggesting higher TCA cycle capacity. We next measured NAD(P)H levels in cultured primary brown adipocytes using live cell fluorescence microscopy. NAD(P)H levels as measured by 450nm emission were 30.8±3.5% higher in PDM compared to CM (Figures 2.4F-G), consistent with CS measurements (Figures 2.4D-E). Taken together, these results suggest that enhanced ATP synthesis and electron transport capacity in PDM are supported by increased substrate oxidation through the TCA cycle.

**Mitochondria-LD contact is decreased upon activation of thermogenic fatty acid oxidation *in vivo***

The reduced fatty acid oxidation capacity observed in isolated PDM suggested that PDM are not specialized for fat oxidation. To determine the relation between PDM and fatty acid oxidation *in vivo*, we next assessed mitochondria-LD contact in BAT harvested from cold-adapted animals, where fatty acid oxidation is maximized to produce heat. If PDM play a significant role in fatty acid oxidation, we predicted that mitochondria-LD contact will be increased in cold-exposed mice compared to mice adapted to thermoneutral conditions, where fatty acids are stored in LDs. Contrary to our predictions, the number of mitochondria in contact with LDs was over 50% lower in cold-exposed mice compared to thermoneutral conditions (Figures 2.4H-I). Quantitative image analysis confirmed this: Mitochondria-LD contact area represented only 3.8±1.0% of mitochondrial perimeter in cold-exposed mice compared to 24.7±3.7% in thermoneutral conditions (Figure 2.4J). To control for reduced LD surface area resulting from lipid oxidation during cold exposure, we quantified mitochondria-LD contact area as a proportion of LD perimeter (Figure 2.4K). Mitochondria-LD contact as a proportion of LD surface was reduced by over 75% in cold exposed animals, confirming that mitochondria-LD contact is reduced by cold exposure. These results suggest that mitochondria-LD contact is negatively associated with fatty acid oxidation *in vivo*.

**Mitochondria-lipid droplet association promotes lipid droplet expansion**

The high level of mitochondria-LD contact observed in thermoneutral conditions led us to hypothesize that mitochondria-LD contact plays a role in LD expansion

rather than oxidation. To test this, we sought to create an experimental system where mitochondrial association to LDs can be induced. Plin5 is a LD-coating protein that is uniquely capable of recruiting mitochondria to LDs (Bosma et al., 2012; H. Wang et al., 2013) through its C-terminal region (Figure 2.5A) (H. Wang et al., 2011). We therefore assessed the effect of adenovirus-mediated Plin5 overexpression on LD expansion in cultured brown adipocytes.

To determine mitochondrial association to LDs we stained transduced cells with TMRE to label the mitochondrial network and BODIPY 493/503 (BODIPY) to label LDs. Confocal microscopy revealed that cells expressing the full version of Plin5 that includes its mitochondrial recruiting sequence (Plin5) significantly increased mitochondrial recruitment to LDs relative to untransduced control cells (Figures 2.5B-C). We confirmed the mitochondrial recruitment phenotype was not due to increased LD content as large areas of the cytosol remained free of LDs and mitochondria in cells over expressing Plin5 (Figures 2.4S, 2.5G).

To control for Plin5 effects that are not related to mitochondrial recruitment, we overexpressed a truncated version of Plin5 that lacks the C-terminal mitochondrial recruiting sequence (Plin5Δ399-463). Confocal imaging confirmed that Plin5Δ399-463 did not significantly increase mitochondrial recruitment to LDs relative to untransduced control cells (Figures 2.5B-C). Next, to determine the effect of Plin5-mediated mitochondrial recruitment to LDs on bioenergetic capacity, we performed respirometry on intact Plin5 transduced cells. Cells expressing the full version of

Plin5 that contains the mitochondrial recruiting sequence had 83.2±24.0% higher ATP-linked respiration and 54.1±28.6% higher spare respiratory capacity compared to cells expressing truncated Plin5Δ399-463 that lacks the mitochondrial recruiting sequence (Figures 2.4S). These results confirmed that mitochondrial recruitment to LDs by Plin5 promotes increased respiratory capacity, in agreement with data from isolated PDM (Figures 2.2A-C).

Next, to determine the effect of mitochondrial recruitment on lipid accumulation, we quantified LD area in confocal microscopy images. Quantitative image analysis revealed that cells expressing the full version of Plin5 that contains mitochondrial recruiting sequence (Plin5) had significantly higher LD accumulation (Figure 2.5D) and size (Figure 2.5E) compared to cells expressing the truncated version of Plin5 that lacks the mitochondrial recruiting sequence (Plin5Δ399-463). We confirmed these effects were not related to lipolysis regulation as overexpression of Plin5 and Plin5Δ399-463 reduced lipolysis to the same extent (Figure 2.5F). These results suggest that mitochondrial association to LDs promotes LD expansion independent of lipolysis regulation.

To determine whether this phenomenon is unique to brown adipocytes, we repeated this experimental series in INS1, a pancreatic beta cell line with low levels of endogenous Plin5 expression and lipogenic capacity (Figure 2.5G). Consistent with brown adipocytes, over 80% of mitochondria were recruited to LDs in INS1 cells expressing Plin5 compared to less than 12% in Plin5Δ399-463 (Figure 2.5H).

Furthermore, LD accumulation and size were significantly higher in INS1 cells expressing Plin5 compared to Plin5Δ399-463 (Figures 2.5I-J). These results suggest that mitochondrial contact with LDs promotes the expansion of LDs in non-adipose cell types.

**Mitochondria-lipid droplet association promotes triacylglyceride synthesis**

We reasoned that mitochondrial recruitment to LDs can expand LDs by enhancing the synthesis of triacylglycerides (TAGs). To test this, we assessed the effect of Plin5 overexpression on TAG synthesis. As before, we performed parallel experiments in cells expressing truncated Plin5Δ399-463 that lacks mitochondrial recruiting sequence but preserve lipolysis regulatory function (Figure 2.4F). Cells were incubated with BODIPY C12 558/568 (C12), a fluorophore-conjugated fatty acid, and thin layer chromatography (TLC) was used to resolve cellular lipid species (Rambold et al., 2015). Plin5 increased C12 incorporation into TAG by 52.1±14.3% while Plin5Δ399-463 increased C12 incorporation by only 11.0±2.5% relative to untransduced controls (Figures 2.6A-B). To confirm C12 incorporation was dependent on TAG synthesis, we incubated cells with Triacsin C, a potent inhibitor of fatty acid esterification into TAG (Figures 2.6C-D). Triacsin C decreased C12 incorporation into TAG by 43.5% and increased free C12 by 28.6%, confirming that C12 incorporation into TAG depends on esterification.

We reasoned that LD recruitment could promote TAG synthesis by fulfilling the energy requirements of ATP-dependent TAG synthesis reactions (Mashek, Li, &

Coleman, 2007; Prentki & Madiraju, 2012). To test this, we assessed the effect of the mitochondrial ATP Synthase inhibitor Oligomycin A on Plin5-enhanced TAG synthesis. C12 incorporation in Plin5 expressing cells was 17.8±3.6% more sensitive to Oligomycin inhibition compared to Plin5Δ399-463 and untransduced controls (Figures 2.6E-F). These results suggest that mitochondrial association to LDs enhance TAG synthesis in a mitochondrial ATP-dependent manner.

**Peridroplet mitochondria have unique structure, fusion dynamics, and movement**

Mitochondria are highly dynamic organelles that continuously undergo cycles of fusion and fission to regulate network morphology and distribute network content (Chen, Chomyn, & Chan, 2005; Liesa & Shirihai, 2013; Nakada et al., 2001). We therefore hypothesized that PDM maintain unique functional and proteomic identity through distinct fusion-fission dynamics. To test this, we first assessed the morphology of PDM and CM in electron micrographs of mice adapted to thermoneutrality, where PDM are the most abundant. Mitochondria with direct contact to LDs had 93.2±22.9% larger cross-sectional area and 47.4±7.3% longer aspect ratio compared to mitochondria with no visible LD association (Figures 2.7A-C). Analysis of internal mitochondrial structure also revealed that cristae in mitochondria associated with LDs were arranged in perpendicular orientation to the axis of mitochondria-LD interface and were 12.0±0.9% shorter and 5.4±0.8% wider compared to mitochondria with no visible association to LDs (Figure 2.5S).

To determine whether PDM structural specializations are preserved in cultured cells, we performed confocal microscopy in living brown adipocytes transduced with mitochondrially-targeted photo-activatable GFP (mtPAGFP). Transduced brown adipocytes were stained with TMRE to visualize the entire mitochondrial network. Individual mitochondria were photo-converted by 2-photon laser pulse and imaged immediately thereafter (Figure 2.7D). Quantitative image analysis confirmed that PDM are more elongated than CM in cultured cells (Figure 2.7E). These results suggest that PDM functional specialization is matched by specialized structure.

We next assessed the fusion activity of CM and PDM in cultured brown adipocytes using mtPAGFP. The dilution of mtPAGFP fluorescence intensity over time reflects fusion of photo-activated mitochondria with non-photo-activated mitochondria. A 150 $\mu m^2$ region of the cell containing primarily PDM or CM was photo-converted by 2-photon laser pulse and imaged continuously at 15-minute intervals. mtPAGFP dilution rate was significantly slower in PDM compared to CM (Figures 7F-G), suggesting that PDM have reduced fusion compared to CM and decreased content exchange with the rest of the mitochondrial network.

We reasoned that reduced PDM fusion could result from a reduction in one or more of the determinants of fusion: 1) Mitofusin (Mfn) expression, 2) mitochondrial membrane potential (MMP), and 3) mitochondrial motility (Twig et al., 2010). Western blot analysis ruled out Mfn expression as the cause of reduced fusion as

Mfn2 expression was high in PDM relative to CM (Figures 2.5S). Additionally, MMP analysis using the membrane potential-sensitive dye TMRE showed that PDM do not have reduced MMP (Figures 2.5S). To determine whether LD association reduces fusion by decreasing mitochondrial motility, we next quantified mitochondrial displacement over time in time-lapse confocal imaging. PDM displacement rate was significantly lower compared to CM (Figures 2.7H-I), suggesting that LD anchoring reduces PDM fusion by arresting motility. Taken together, these results suggest that PDM have reduced mitochondrial motility leading to decreased fusion activity that promotes their segregation from CM.

**Peridroplet mitochondria have reduced DRP1 recruitment and OPA1 processing**

The concomitant reduction in PDM fusion activity and marked elongation led us to hypothesize that reduced fusion rate is matched by reduced fission activity (Chen et al., 2003). To assess outer membrane fission, we measured the recruitment of DRP1 to mitochondria by immunofluorescence (Cereghetti et al., 2008). Drp1 was immunolabeled in cultured cells where the mitochondrial network was labelled by mitochondrially-targeted DsRed (mtDsRed). Confocal imaging revealed significantly lower DRP1 staining on PDM compared to CM (Figures 2.8A-B), suggesting lower outer membrane fission activity. Next, to assess inner membrane fission, we measured OPA1 processing in isolated mitochondria. Proteolytic cleavage of the long-forms OPA1 (L-OPA1) to short-OPA1 (S-OPA1) is associated

with inner membrane fission (Anand et al., 2014). Western blot analysis revealed significantly lower levels of S-OPA1 in PDM compared to CM, suggesting lower inner membrane fission activity (Figures 2.8C-F). We reasoned that fission arrest can be a cause or a consequence of LD recruitment. To test this, we assessed mitochondrial LD association in cells expressing the dominant-negative DRP1 K38A (DRP1DN)(Smirnova, Griparic, Shurland, & van der Bliek, 2001). DRP1DN did not enhance mitochondrial recruitment to LDs (Figures 2.8G-H), suggesting that fission arrest is a consequence rather than a cause of LD recruitment. Taken together, these results suggest that LD association reduces fission protein recruitment and processing that promotes PDM elongation.

## Discussion

### Peridroplet mitochondrial isolation by differential centrifugation

In this study we developed an approach to isolate intact respiring PDM and determine their bioenergetic function for the first time. Our approach took advantage of the buoyancy of LDs to separate LD-bound PDM from CM. PDM were then purified using high-speed centrifugation, a procedure previously shown to strip LD-associated proteins (Figure 2.1) (Ding et al., 2013; Yu et al., 2015). These results raise important considerations for the interpretation of past and future experiments with isolated mitochondria. First, mitochondrial isolation protocols that eliminate lipid fraction by aspiration (Rogers et al., 2011) and/or

gauze filtration (Cannon & Nedergaard, 2001) may miss physiologically relevant changes that occur in PDM but not in CM. Second, isolation protocols that include an initial high-speed centrifugation step prior to low-speed centrifugation steps (Cannon & Nedergaard, 2001; Djafarzadeh & Jakob, 2017) may inadvertently strip LDs, resulting in a mixed population of CM and PDM. To our knowledge, this is the first report to specifically isolate intact respiring PDM from any tissue type and directly determine their functional role.

**PDM have specialized oxidative phosphorylation protein composition and capacity**

BAT mitochondria isolated by previous methods were shown to have low levels of ATP synthase elementary particles (Lindberg, de Pierre, Rylander, & Afzelius, 1967) and activity (Cannon & Vogel, 1977). Our study reveals that PDM have over two-fold higher ATP synthesis capacity matched by enriched ATP synthase protein subunits when compared to CM, which may explain the relatively low levels of ATP synthesis reported in mitochondria isolated from BAT using previous methods. Consistent with higher ATP synthesis capacity, PDM were also enriched with cytochrome c oxidase and had increased electron transport capacity (Figure 2.3). We confirmed that higher respiration was not due to an artefactual difference in mitochondrial enrichment of PDM fraction by mass spectrometry analysis (Figure 2.1H) and imaging of mitochondria loaded within seahorse XF96 plates (Figures 2.2A-B). In addition, careful attention was dedicated to eliminate potential artifacts

due to the presence of free fatty acids. Free fatty acids can alter respiration by 1) providing fuel for beta oxidation, 2) acting as weak uncouplers (Y. Li, Fromme, Schweizer, Schöttl, & Klingenspor, 2014), and 3) activating UCP1 (Fedorenko, Lishko, & Kirichok, 2012). To address this, we assessed the lipid contents of CM and PDM (Figures 2.1F-G) and supplemented the respiratory buffer with 0.1% BSA to remove free fatty acids from solution as well as 1mM of the UCP1 inhibitor GDP. ADP- and FCCP-stimulated respiration confirmed that mitochondria were coupled at the start of the assay. Free fatty acids could not serve as mitochondrial fuels in this system because the enzymes and cofactors required for acyl-CoA and acyl-carnitine syntheses are not present in assay buffer. Our results thus demonstrate that PDM represents a mitochondrial subpopulation with distinct bioenergetics and protein composition.

**Peridroplet mitochondria are segregated by reduced fusion-fission dynamics**

In every cell type where mitochondrial dynamics has been studied, mitochondria were shown to go through continuous cycles of fusion and fission that equilibrate the mitochondrial content across the mitochondrial population of the cell. We have previously reported that mitochondria in brown adipocytes continuously engage in fusion and fission activities (Wikstrom et al., 2014). The mechanism by which mitochondrial subpopulations can maintain separate function and composition in brown adipocytes was therefore unclear. Disparate mitochondrial subpopulations

have been previously observed in tissues where mitochondrial subpopulations are separated in space (Wikstrom, Twig, & Shirihai, 2009). For example, in striated muscle, it has been observed that subsarcolemmal mitochondria that are separated from interfibrillar mitochondria by the sarcomere have specialized form and function (Palmer, Tandler, & Hoppel, 1977). However, the brown adipocyte lacks the cytoplasmic subdivision that is mediated by myocyte sarcomeres and thus one expects fusion and fission to continuously equilibrate mitochondrial content across the adipocyte mitochondrial population (Wikstrom et al., 2014). Our results demonstrate that PDM have reduced fusion-fission dynamics that segregate them from the rest of the mitochondrial population (Figures 2.7F-G). Various evidence support that altered mitochondrial dynamics are a consequence rather than a cause of LD recruitment: 1) Neither fusion arrest (Boutant et al., 2017) nor fission arrest (Figures 2.8G-H) recruit mitochondria to LDs and 2) Mitochondrial recruitment to LDs by Plin5 promotes mitochondrial elongation (H. Wang et al., 2013). This supports the conclusion that reduced mitochondrial dynamics are a consequence rather than a cause of LD association. Furthermore, our observation that PDM are stationary (Figures 2.7H-I) suggests a mechanism by which LD association reduces mitochondrial dynamics, as we have previously shown that stationary mitochondria have markedly lower probability to undergo fusion (Twig et al., 2008, 2010). Our results thus suggest that PDM maintain functional and

proteomic segregation from CM by having reduced motility and fusion-fission dynamics.

**Peridroplet mitochondria are not associated with fatty acid oxidation**

Recent studies have hypothesized that PDM facilitate fatty acid trafficking toward mitochondrial beta oxidation (Boutant et al., 2017; Rambold et al., 2015) while others have suggested that mitochondria-LD association enhances LD biogenesis and thereby protects mitochondria from lipotoxicity (Nguyen et al., 2017; Stone et al., 2009, p. 2; H. Wang et al., 2011). In this study we employed brown adipose tissue, a system that robustly shifts from LD expansion under thermoneutral conditions to lipid oxidation under cold/adrenergic stimulus. If PDM facilitate fat oxidation, we reasoned mitochondria-LD association will increase during cold-induced thermogenesis, when fatty acid oxidation rate is maximal. However, contrary to the hypothesis, mitochondrial association with LDs was decreased by cold-exposure (Figures 2.4H-K). These results are consistent with the previously published observation that mitochondrial protein content is reduced in LDs isolated from BAT of cold-adapted mice compared to mice in thermoneutral environment (Yu et al., 2015). Our analyses of isolated mitochondria confirmed that PDM have lower fatty acid oxidation capacity and higher TCA cycle capacity compared to CM (Figures 2.4A-G). Taken together, these results support the conclusion that PDM are not specialized for lipid oxidation in BAT.

**Mitochondria-lipid droplet interaction enhances lipid droplet expansion**

The high level of mitochondria-LD contact observed in BAT under thermoneutral conditions led us to hypothesize that PDM play a role in LD expansion. To test this, we induced mitochondrial recruitment to LDs using adenoviral-mediated Plin5 overexpression, which has been shown to recruit mitochondria to LDs in multiple cell and tissue types (Bosma et al., 2012; H. Wang et al., 2011, 2013). Importantly, we developed a system in which the specific effects of mitochondrial recruitment can be differentiated from other Plin5 effects, such as lipolytic regulation. Our 2.results show that mitochondrial recruitment to LDs doubled the size of LDs (Figure 2.5). Furthermore, the capacity of PDM to promote the incorporation of free fatty acids into TAG was dependent on mitochondrial ATP synthesis (Figure 2.6). This observation supports the conclusion that PDM enhance LD expansion by providing ATP to the ATP-demanding process of acyl-CoA synthesis and lipid cycling (Prentki & Madiraju, 2012). In addition, the increased TCA cycle capacity we observed suggests that PDM may support LD expansion by providing citrate for de novo lipogenesis. Taken together, our results thus support the conclusion that PDM support LD expansion rather than oxidation.

We suggest that increased mitochondrial recruitment to LDs may be part of a generalized adaptive response in physiological conditions that require LD expansion, such as post-prandial lipid synthesis and storage. PDM-mediated LD expansion may also play a role in muscle and liver injury from lipotoxicity in conditions of nutrient excess, such as obesity and hyperlipidemia. A better

understanding of PDM and LD biology may therefore be important for developing new therapies for lipotoxic tissue injury and insulin resistance. Animal models in which mitochondria-LD association can be specifically modulated will be necessary to resolve such questions in future studies.

**Limitations of study**

This study is the first to isolate intact respiring PDM and determine their unique composition and bioenergetics. However, our study has several limitations. Limitations of our PDM isolation approach include: 1. Mitochondrial isolation by differential centrifugation results in relatively crude preparations contaminated with other organelles and cellular compartments. Mass spectrometry analysis of CM and PDM preparations revealed that approximately half of the proteins present in CM and PDM preparations were mitochondrial (Figure 2.1H), in agreement with previously published reports (Forner et al., 2009). 2. Mitochondrial isolation by differential centrifugation pools all PDM into a single pellet. As such, inter-mitochondrial heterogeneity (Figures 2.3F-I) is lost in subsequent biochemical and functional assays, which may lead to under-estimation of differences between CM and PDM populations (Figures 2.3A-C). 3. PDM isolation by differential centrifugation may preferentially select for PDM attached to larger LDs with higher buoyancy. Small LDs with insufficient buoyancy could potentially contaminate the supernatant and CM pellet and lead to further under-estimation of the differences between isolated CM and PDM properties. 4. Our method used high-speed

centrifugation to strip PDM from LDs, a procedure which may alter their function. However the close agreement between our proteomic and bioenergetic data in living cells and isolated mitochondria (Figures 2.2-3) suggests that isolated PDM preserved the metabolic phenotype observed in intact cells.

**Figures**

**Figure 2.1. Isolation of peridroplet mitochondria by differential centrifugation.**

A. Schematic representation of peridroplet (PDM) and cytoplasmic (CM) mitochondrial isolation from interscapular brown adipose tissue (BAT). BAT was dissected from mice and homogenized with glass-Teflon dounce homogenizer. Low-speed centrifugation separated the fat layer containing PDM from supernatant containing CM. High-speed centrifugation stripped PDM from lipid droplets (LDs) and pelleted CM mitochondria from the supernatant. Note that some BAT mitochondrial isolation protocols discard the fat layer and/or begin with high-speed centrifugation step.

B-E. PDM are stripped from LDs by high-speed centrifugation.

B-C. Super-resolution confocal images of the fat layer before and after high-speed centrifugation. LDs were marked by the neutral BODIPY 493/503 fluorescent dye (BODIPY) and mitochondria by MitoTracker deep red dye (MitoTracker). Note the tubular structures staining positively for MitoTracker on LDs.

D. Quantification of LDs with MitoTracker staining in the fat layer pre- and post-stripping by high-speed centrifugation. 11,744 LDs were assessed in total. *** $p < 0.0001$.

E. Super-resolution confocal image of PDM pellet separated from fat layer by high-speed centrifugation.

F-G. Low-magnification (20x) images of the fat layer, PDM pellet, and CM pellet. LD content was assessed by BODIPY staining. 5-6 technical replicates per group. N = 3 independent isolations. ns $p>0.05$, *** $p < 0.0001$. One-way ANOVA with Tukey post-test.

H. Mass spectrometry analysis of relative mitochondrial protein content of CM and PDM preparations.

I-J. Analysis of CM and PDM membrane potential by fluorescence microscopy of CM and PDM double-stained with the membrane potential-sensitive dye MitoTracker Red and the mitochondrial protein dye MitoTracker Green. N = 15-22 images per group from 3 independent isolations. ns $p>0.05$.

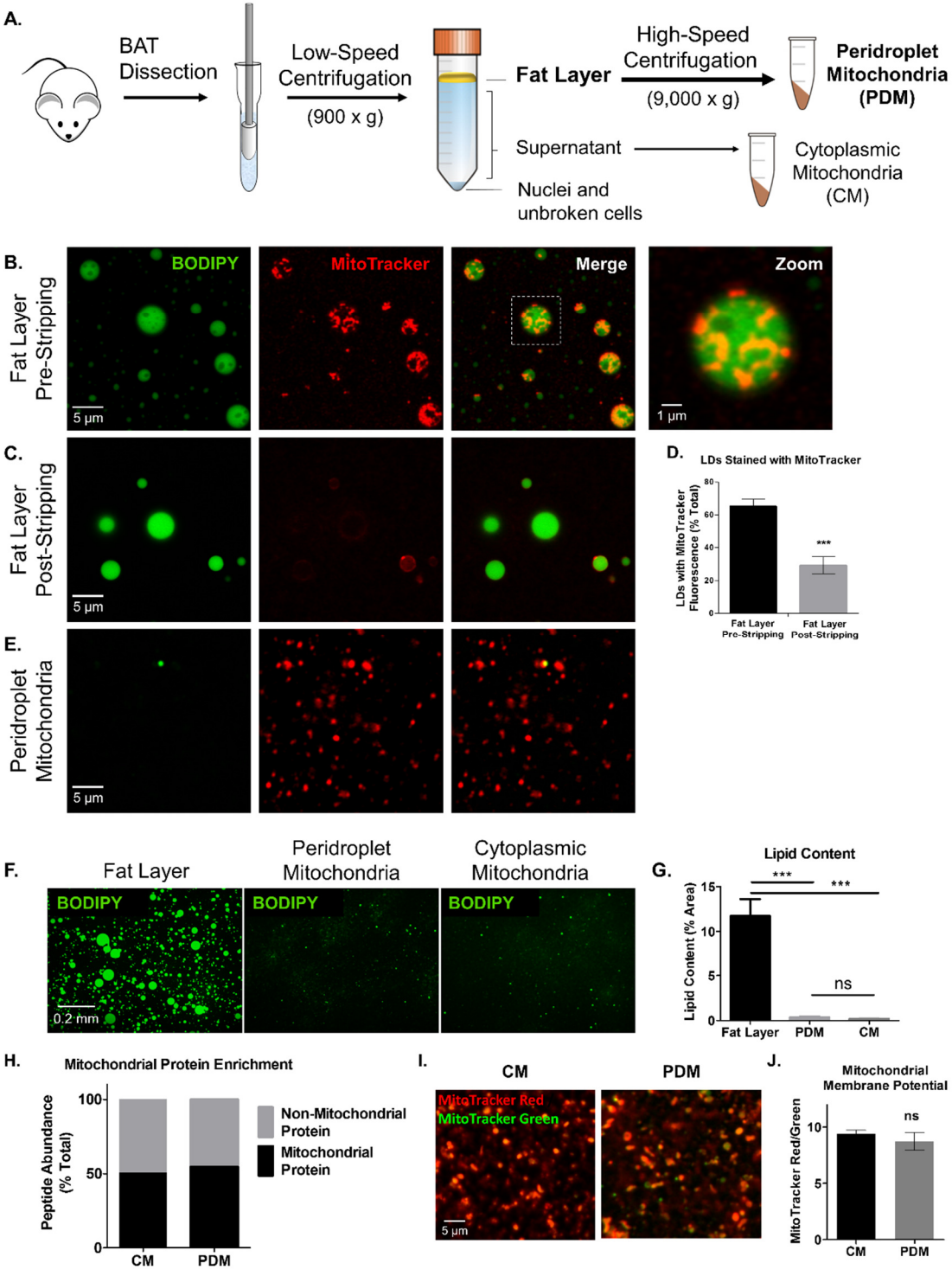
A.
BAT Dissection
Low-Speed Centrifugation
(900 x g)
Fat Layer
High-Speed Centrifugation
(9,000 x g)
Peridroplet Mitochondria (PDM)
Supernatant
Cytoplasmic Mitochondria (CM)
Nuclei and unbroken cells
B.
Fat Layer Pre-Stripping
BODIPY
MitoTracker
Merge
Zoom
5 µm
1 µm
C.
Fat Layer Post-Stripping
5 µm
D.
LDs Stained with MitoTracker
LDs with MitoTracker Fluorescence (% Total)
***
Fat Layer Pre-Stripping
Fat Layer Post-Stripping
E.
Peridroplet Mitochondria
5 µm
F.
Fat Layer
Peridroplet Mitochondria
Cytoplasmic Mitochondria
BODIPY
0.2 mm
G.
Lipid Content
Lipid Content (% Area)
***
ns
Fat Layer
PDM
CM
H.
Mitochondrial Protein Enrichment
Peptide Abundance (% Total)
Non-Mitochondrial Protein
Mitochondrial Protein
CM
PDM
I.
CM
PDM
MitoTracker Red
MitoTracker Green
5 µm
J.
Mitochondrial Membrane Potential
MitoTracker Red/Green
ns
CM
PDM

**Figure 2.2. Peridroplet mitochondria have enhanced bioenergetic capacity.**

A-I. Peridroplet (PDM) and cytosolic (CM) mitochondria isolated from brown adipose tissue (BAT).

A. Fluorescence microscopy images of seahorse respirometry plate wells containing isolated CM and PDM stained with MitoTracker Red.

B. Quantification of MitoTracker Red fluorescence intensity (F.I.) in Seahorse wells loaded with CM or PDM. 5-7 wells quantified per condition.

C. Representative traces of oxygen consumption rates (OCRs) of isolated PDM and CM driven with pyruvate+malate. ADP, Oligomycin, FCCP, and Antimycin were sequentially injected to assess mitochondrial respiratory states. 4-6 technical replicates per group.

D. Quantification of OCR at different mitochondrial respiratory states in representative experiment. State II quantifies respiration driven proton leak (no ATP synthesis), State III quantifies respiration driven by ATP synthesis, and maximal respiration quantifies maximal electron transport activity induced by the chemical uncoupler FCCP. 6 technical replicates per group.

E. Quantification of mitochondrial respiratory states in N = 8 independent experiments. For each individual experiment, average OCR values of CM and PDM were normalized to the average OCR of all mitochondria (see Quantification and Statistical Analysis for complete equations).

F-G. Cytochrome C oxidase activity in PDM and CM isolated from BAT.

F. Representative traces of oxygen consumption rate (OCR) of isolated PDM and CM driven with the cytochrome c oxidase-specific substrates TMPD+Ascorbate. Rotenone and Antimycin were injected in the beginning of the assay to extinguish cytochrome c reduction by Complex I and Complex III. The COX-specific inhibitor sodium azide was injected at the end of the assay to control for non-COX oxygen consumption. 5 technical replicates per group.

G. Quantification of COX activity in N = 4 independent isolations. Data were normalized as in E.

H-I. ATP synthase activity in PDM and CM isolated from BAT.

H. Representative traces of luciferase luminescence assay in isolated mitochondria normalized to baseline. ATP synthesis rates were determined by the rate of luminescence gain.

I. Quantification of ATP synthase activity in N = 4 independent isolations. Data were normalized as in E.

J-K. Confocal imaging of living cultured brown adipocytes stained with membrane potential-sensitive dye TMRE.

J. Confocal imaging before and after addition of the ATP synthase inhibitor oligomycin. Bright field image was used to identify LDs. TMRE images were pseudo-colored for quantitative display (see calibration bar in top left). Note that PDM had higher fluorescence than CM after oligomycin treatment. White dashed

circles denote LDs, white N denotes the nucleus, and white square denotes zoomed region.

K. Quantification of TMRE fluorescence intensity in oligomycin-treated brown adipocytes. 159 mitochondria were assessed in total. N = 33 cells collected in 6 independent experiments.

Data are expressed as means ± SEM. ns $p>0.05$, * $p< 0.05$, ** $p < 0.001$, *** $p < 0.0001$.

See also Figure 2.1S.

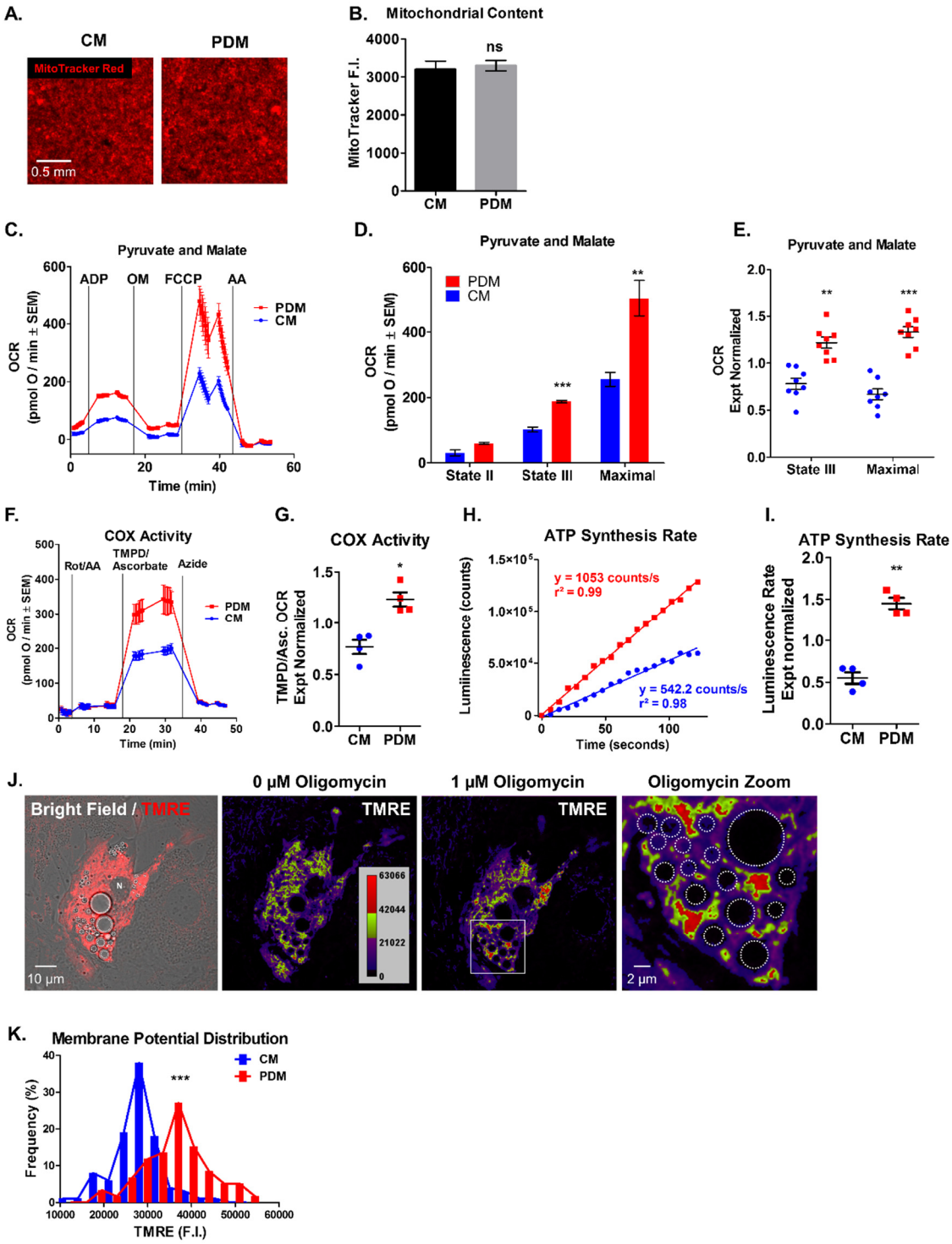
A.
CM
PDM
MitoTracker Red
0.5 mm
B.
Mitochondrial Content
MitoTracker F.I.
ns
CM
PDM
C.
Pyruvate and Malate
OCR (pmol O / min ± SEM)
ADP
OM
FCCP
AA
PDM
CM
Time (min)
D.
Pyruvate and Malate
OCR (pmol O / min ± SEM)
PDM
CM
State II
State III
Maximal
E.
Pyruvate and Malate
OCR Expt Normalized
State III
Maximal
F.
COX Activity
OCR (pmol O / min ± SEM)
Rot/AA
TMPD/ Ascorbate
Azide
PDM
CM
Time (min)
G.
COX Activity
TMPD/Asc. OCR Expt Normalized
CM
PDM
H.
ATP Synthesis Rate
Luminescence (counts)
y = 1053 counts/s
r² = 0.99
y = 542.2 counts/s
r² = 0.98
Time (seconds)
I.
ATP Synthesis Rate
Luminescence Rate Expt normalized
CM
PDM
J.
Bright Field / TMRE
0 µM Oligomycin
1 µM Oligomycin
Oligomycin Zoom
TMRE
63066
42044
21022
0
10 µm
2 µm
K.
Membrane Potential Distribution
Frequency (%)
CM
PDM
TMRE (F.I.)

**Figure 2.3. Peridroplet mitochondria have increased levels of cytochrome c oxidase, ATP synthase and super complex I+III assembly.**

A-C. Western blot analysis of Peridroplet (PDM) and cytosolic (CM) mitochondria isolated from brown adipose tissue (BAT).

A. Western blot of isolated CM and PDM stained with the dye Ponceau S for total protein loading.

B. Western blot probed with antibodies of OXPHOS complex subunits I-V (CI-CV) and TOM20 as a loading control.

C. Quantification of OXPHOS complex subunits normalized to TOM20 loading control in N = 4-7 independent isolations. For each individual experiment, average values detected in CM and PDM were normalized to the average protein subunit levels of all mitochondria (see Quantification and Statistical Analysis for complete equations).

D-E. Western blot of Blue Native PAGE of PDM and CM isolated from BAT.

D. Western blot of assembled complex I and complex III in isolated mitochondria.

E. Quantification of complex III assembled into I+III supercomplexes relative to total complex III. N = 5 independent isolations. Data were normalized as in C.

F-I. Super-resolution confocal imaging of fixed cultured brown adipocytes (no adrenergic stimulation).

F. Brown adipocytes immunostained for cytochrome c oxidase subunit 4 (COX4). Bright field image was used to identify LDs and TOM20 immunostaining was used

to mark the mitochondrial network. White dashed circles denote LDs, white N denotes the nucleus, and white square denotes zoomed region.

G. Quantification of COX4 distribution in brown adipocyte mitochondria. 490 mitochondria were assessed in total. N = 22 cells collected in 3 independent experiments.

H. Brown adipocytes immunostained for ATP Synthase. Bright field image was used to identify LDs and TOM20 immunostaining was used to mark the mitochondrial network. White dashed circles denote LDs, white N denotes the nucleus, and white square denotes zoomed region.

I. Quantification of ATP Synthase distribution in brown adipocyte mitochondria. 507 mitochondria were assessed in total. N = 20 cells collected in 4 independent experiments.

Data are expressed as means ± SEM. * $p < 0.05$, *** $p < 0.0001$.

See also Figure 2.2S.

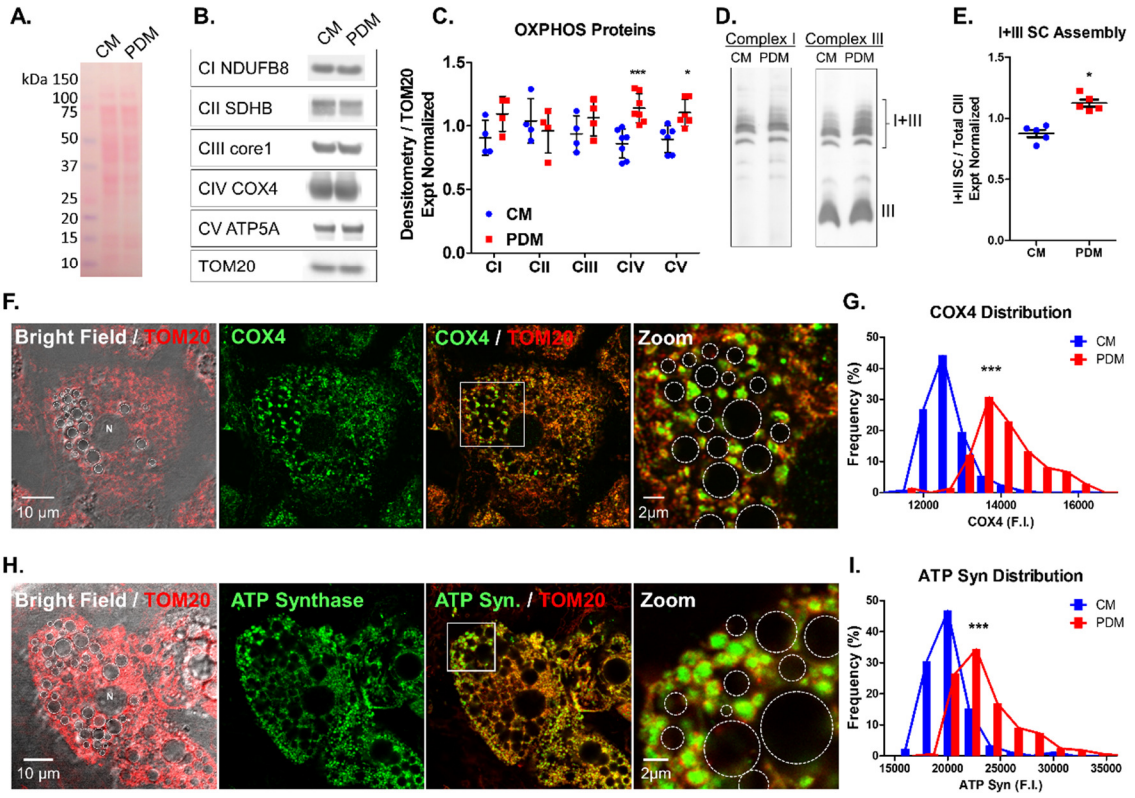


**Figure 2.4. Peridroplet mitochondria have decreased fatty acid oxidation capacity and mitochondria-LD contact is decreased upon activation of thermogenic fatty acid oxidation *in vivo*.**

A. PDM have lower fatty acid oxidation capacity. Representative quantification of maximal palmitoyl-carnitine driven oxygen consumption rate (Max OCR) in isolated peridroplet (PDM) and cytoplasmic (CM) mitochondria. 4-6 technical replicates per group.

B. Quantification of palmitoyl-carnitine oxidation capacity. N = 5 independent experiments. For each individual experiment, average OCR values of CM and

PDM were normalized to the average OCR of total mitochondria (see Quantification and Statistical Analysis for full equations).

C. UCP1 protein is similarly abundant in PDM and CM. Western blot analysis of UCP1 in CM and PDM. N = 3 independent mitochondrial isolations. Data were normalized as in B.

D-E. PDM have higher activity of the TCA cycle enzyme Citrate Synthase.

D. Representative traces of citrate synthase DTNB absorbance assay in isolated mitochondria normalized to baseline. Citrate synthase activity was determined for CM and PDM by the rate of absorbance gain.

E. Quantification of citrate synthase specific activity. N = 4 independent mitochondrial isolations. Data were normalized as in B.

F-G. PDM have increased NAD(P)H content.

F. Confocal image of NAD(P)H fluorescence in living cultured brown adipocytes. Image was pseudo-colored for quantitative display (see calibration bar in top left). Note the high level of NAD(P)H in PDM.

G. Quantification of NAD(P)H level. N = 24 cells imaged in 6 independent experiments. CM and PDM fluorescent intensities (F.I.) were normalized to average cell F.I. for each individual cell.

H. Electron micrographs (EMs) of BAT harvested from mice adapted to thermoneutral conditions (28°C), where fatty acids are stored in lipid droplets, and cold environment (6°C), where thermogenic fatty acid oxidation is robustly

increased. Blue lines highlight mitochondrial perimeter and red lines highlight overlap between mitochondria and lipid droplet border.

I-K. Mitochondria in contact with lipid droplets were quantified by count, % mitochondrial perimeter and % lipid droplet perimeter. N = 10 EMs per condition. Data are expressed as means ± SEM. ns $p>0.05$, * $p< 0.05$, ** $p < 0.001$, *** $p < 0.0001$.

See also Figure 2.3S.

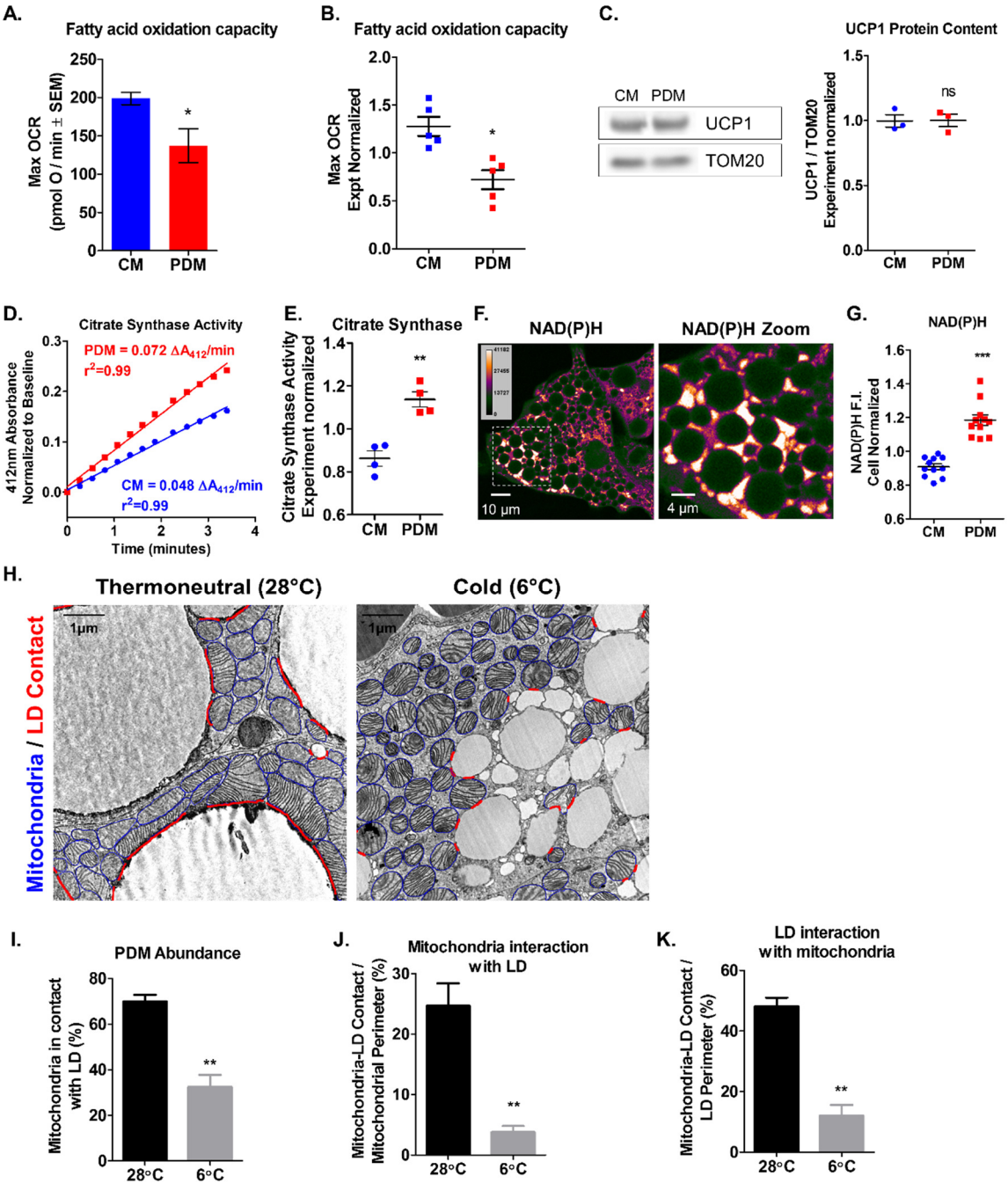


**Figure 2.5. Mitochondria-lipid droplet association promotes lipid droplet expansion.**

A. Schematic representation of Perilipin5 (Plin5) domains: the conserved perilipin domains PAT1 and PAT2, the ATGL-binding domain responsible for lipolysis regulation, and the mitochondrial recruiting sequence.

B. Super-resolution confocal images of living brown adipocytes untransduced (control), transduced with the full-length Plin5 that contains mitochondrial recruiting sequence (Plin5), and transduced with truncated Plin5 that lacks the mitochondria recruitment sequence (Plin5Δ399-463). Mitochondria are marked by TMRE staining and lipid droplets (LDs) by BODIPY 493/503. Note the increased lipid droplet (LD) mass and mitochondrial recruitment in Plin5-transduced cells.

C. Quantification of mitochondrial recruitment to LDs assessed as the area of mitochondria within 0.5 μm of LD border. N = 14-24 cells analyzed per group from 4 independent experiments.

D. Quantification of LD mass by cross-sectional area of BODIPY 493/503 normalized to cell area. N = 17-33 cells per group from 4 independent experiments.

E. LD size distribution assessed by cross-sectional area of individual LDs. N = 302-489 LDs per group from 4 independent experiments.

F. Quantification of lipolysis by glycerol release assay. N = 3 independent experiments. For each individual experiment, average values of CM and PDM were normalized to the average values of total mitochondria (see Quantification and Statistical Analysis for full equations).

G. Super-resolution confocal images of living INS1 pancreatic beta cell line untransduced (control), transduced with Plin5, and Plin5Δ399-463 and stained with TMRE to mark mitochondria and BODIPY 493/503 to mark LDs. Note the increased LD mass and mitochondrial recruitment in Plin5.

H. Quantification of mitochondrial recruitment to LDs assessed as the area of mitochondria within 0.5 µm of LD border. N = 12-20 cells analyzed per group from 3 independent experiments.

I. Quantification of LD mass by cross-sectional area of BODIPY 493/503 normalized to cell area. N = 13-19 cells per group from 3 independent experiments.

J. LD size distribution assessed by cross-sectional area of individual LDs. N = 226-344 LDs per group from 3 independent experiments.

Data are expressed as means ± SEM. ns $p>0.05$, * $p< 0.05$, ** $p < 0.001$, *** $p < 0.0001$.

See also Figure 2.4S.

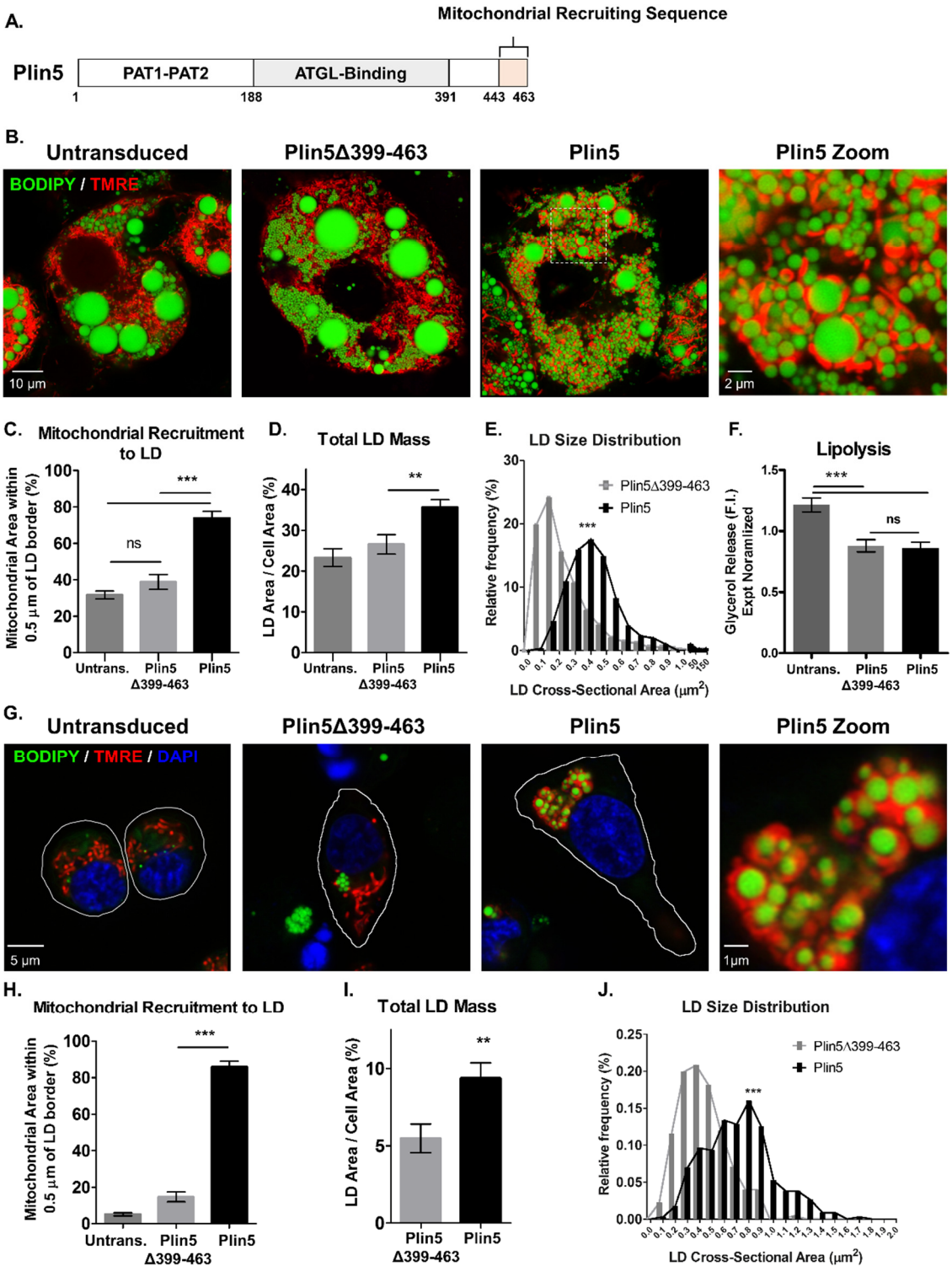
A.
Mitochondrial Recruiting Sequence
Plin5
PAT1-PAT2
ATGL-Binding
1
188
391
443
463
B.
Untransduced
Plin5Δ399-463
Plin5
Plin5 Zoom
BODIPY / TMRE
10 μm
2 μm
C.
Mitochondrial Recruitment to LD
Mitochondrial Area within 0.5 μm of LD border (%)
ns
***
Untrans.
Plin5 Δ399-463
Plin5
D.
Total LD Mass
LD Area / Cell Area (%)
**
E.
LD Size Distribution
Plin5Δ399-463
Plin5
Relative frequency (%)
LD Cross-Sectional Area (μm²)
F.
Lipolysis
Glycerol Release (F.I.) Expt Noramlized
ns
G.
Untransduced
Plin5Δ399-463
Plin5
Plin5 Zoom
BODIPY / TMRE / DAPI
5 μm
1μm
H.
Mitochondrial Recruitment to LD
I.
Total LD Mass
J.
LD Size Distribution

**Figure 2.6. Mitochondria-lipid droplet association promotes triacylglyceride synthesis.**

A. Representative thin layer chromatography (TLC) of cellular lipids extracted from cultured brown adipocytes untransduced (control), transduced with the full-length Plin5 that contains mitochondrial recruiting sequence (Plin5), and truncated Plin5 that lacks the mitochondria recruitment sequence (Plin5Δ399-463). Cells were incubated with BODIPY C12 558/568 (C12) overnight to assess triacylglyceride (TAG) synthesis. The mobility of fatty acids species from loading origin is determined by relative polarity, with TAG migrating the highest.

B. Quantification of TAG from N = 3 independent experiments. Data were normalized to control for each individual experiment.

C-D. TLC of cultured brown adipocytes incubated with C12 with or without the fatty acid esterification inhibitor Triacsin C (red). In histogram, note the decrease in TAG and increase in Free C12 induced by Triacsin C.

E. Representative TLC of cultured brown adipocytes incubated with C12 with or without the mitochondrial ATP synthase inhibitor oligomycin.

F. Quantification of TAG synthesis dependent on mitochondrial ATP from N = 3 independent experiments. Mitochondrial ATP-dependent TAG synthesis was calculated as the difference in TAG between oligomycin-treated and untreated cells.

Data are expressed as means ± SEM. * $p < 0.05$, ** $p < 0.001$.

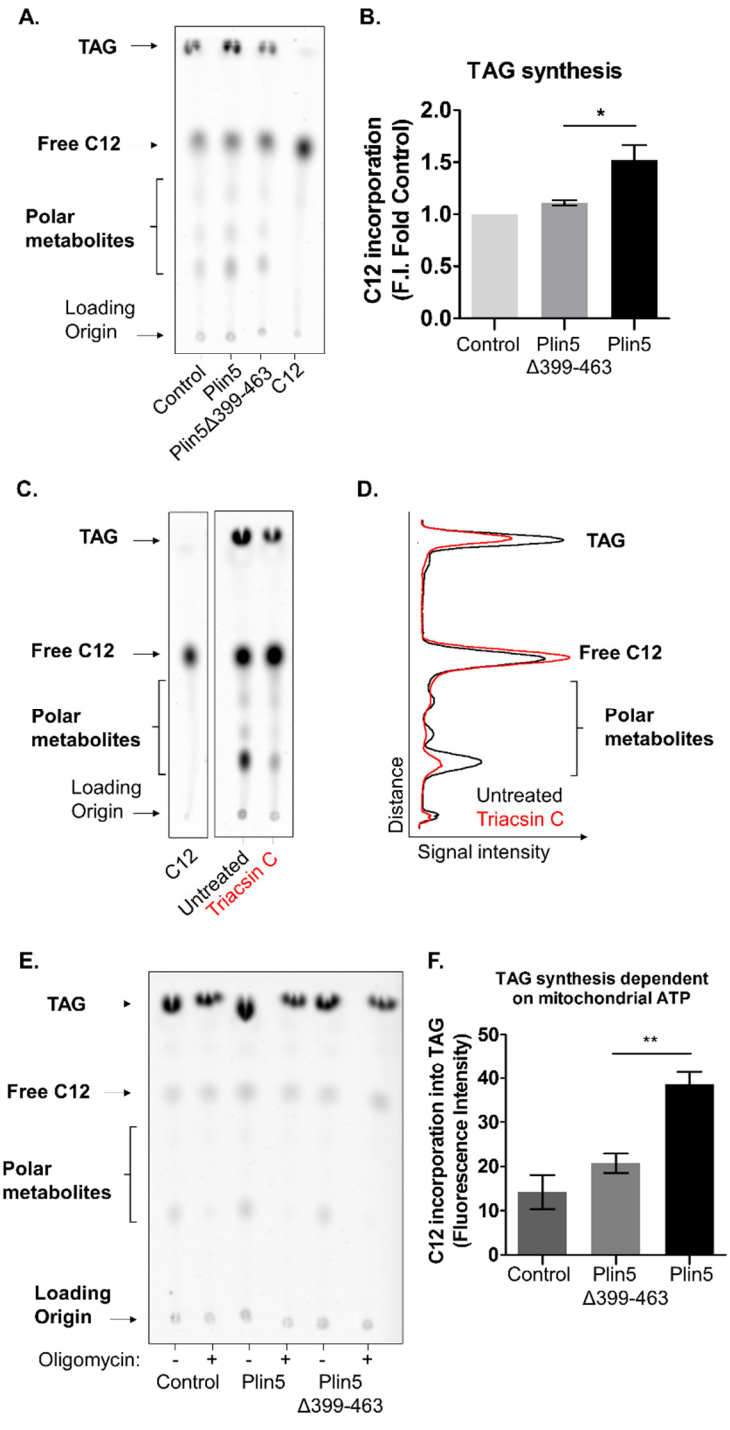
A.
TAG
Free C12
Polar metabolites
Loading Origin
Control
Plin5
Plin5Δ399-463
C12
B.
TAG synthesis
C12 incorporation (F.I. Fold Control)
2.0
1.5
1.0
0.5
0.0
*
Control
Plin5
Plin5 Δ399-463
C.
TAG
Free C12
Polar metabolites
Loading Origin
C12
Untreated
Triacsin C
D.
TAG
Free C12
Polar metabolites
Distance
Untreated
Triacsin C
Signal intensity
E.
TAG
Free C12
Polar metabolites
Loading Origin
Oligomycin: - + - + - +
Control
Plin5
Plin5 Δ399-463
F.
TAG synthesis dependent on mitochondrial ATP
C12 incorporation into TAG (Fluorescence Intensity)
50
40
30
20
10
0
**
Control
Plin5
Plin5 Δ399-463

**Figure 2.7. Peridroplet mitochondria have unique structure, fusion-fission dynamics, and motility.**

A-C. Electron micrograph (EMs) of BAT harvested from mice adapted to thermoneutral conditions (28°C), where peridroplet mitochondria (PDM) are most abundant. Red lines highlight PDM and blue lines highlight cytoplasmic mitochondria (CM). Note the elongation of PDM. Mitochondrial size and shape were quantified in N = 22 – 34 mitochondria from 10 EMs per group.

D-E. Confocal microscopy of living cultured brown adipocytes.

D. Confocal images of brown adipocytes transduced with mitochondrially-targeted photo-activatable GFP (mtPAGFP) stained with TMRE to label the mitochondrial network. mtPAGFP in single mitochondria (white squares) were sequentially photo-converted and imaged immediately. Filled grey circles denote lipid droplets.

E. Quantification of mitochondrial shape, as delineated by mtPAGFP. N = 47 mitochondria from 4 independent imaging experiments.

F-G. Mitochondrial fusion assay image and quantification in living cultured brown adipocytes. Brown adipocytes transduced mtPAGFP were stained with TMRE to label the mitochondrial network. White dashed circles denote LDs and white N denotes the nucleus. mtPAGFP was photo-converted in a small region of the cell (white squares) and its fluorescence intensity tracked over time. The dilution of mtPAGFP fluorescence intensity over time results from fusion between activated mitochondria with non-activated mitochondria. N = 5 cells per group imaged in 3

independent experiments. Data were normalized to baseline and statistically analyzed by Two-Way ANOVA for repeated measures with Bonferroni post-test.

H-I. PDM have reduced motility compared to CM.

H. Psudo-colored confocal images of brown adipocyte at two different time points (red and green). Merged image of two time points reveals immobile mitochondria (yellow) and mobile mitochondria that change position over time (red and green). White dashed circles denote LDs, white N denotes the nucleus, and white dashed square denotes zoomed region. Note the reduced mobility of PDM compared to CM.

I. Quantification of mitochondrial motility. Mitochondrial motility was quantified in time-lapse images as the percent of area displaced over a period of 10 seconds. For each individual cell, CM and PDM motility values were normalized to the average motility value of all mitochondria in the cell. N = 15 cells images in 3 independent experiments.

Data are expressed as means ± SEM. * $p < 0.05$, *** $p < 0.0001$.

See also Figure 2.5S.

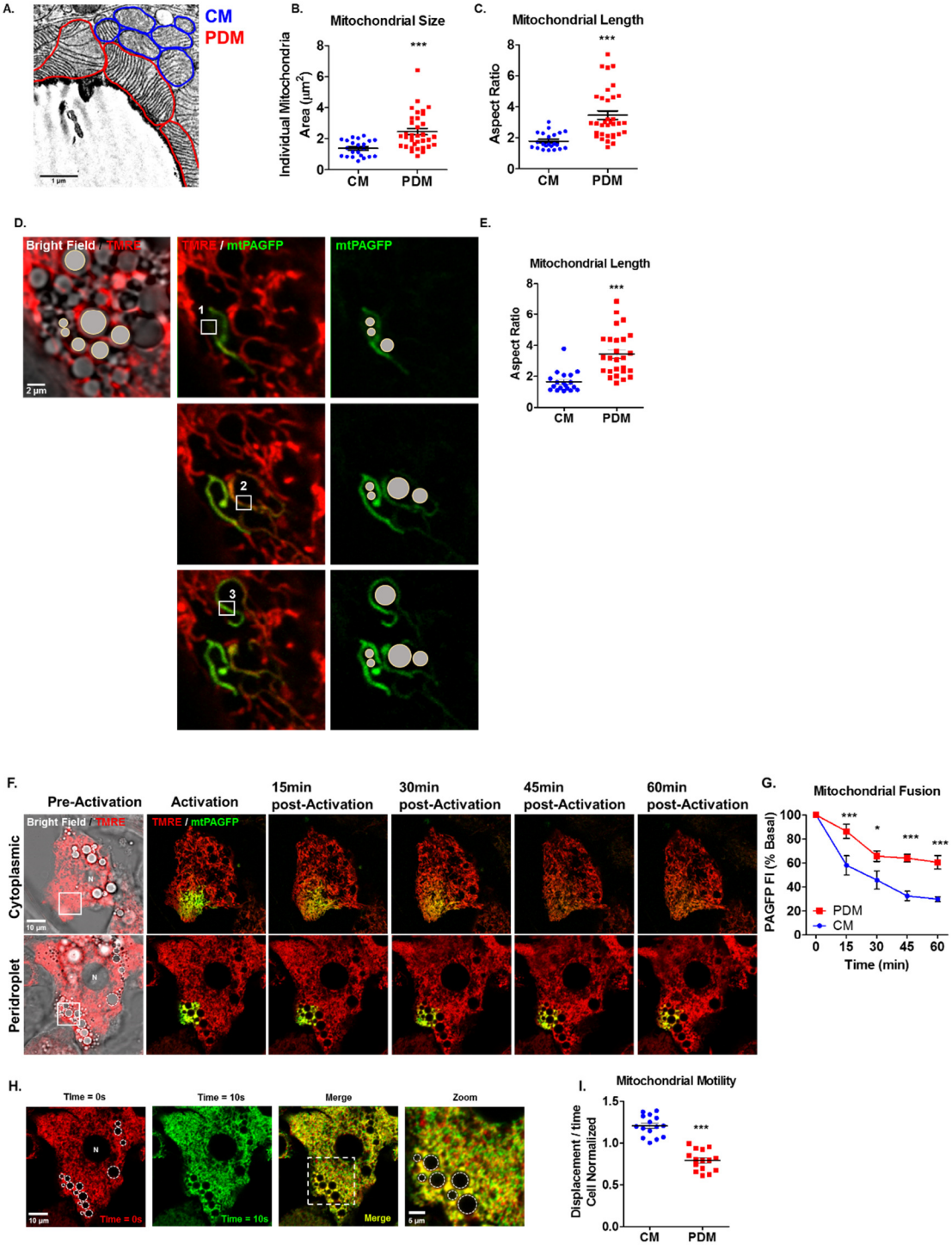
A.
CM
PDM
B.
Mitochondrial Size
Individual Mitochondria Area (μm²)
***
CM
PDM
C.
Mitochondrial Length
Aspect Ratio
***
CM
PDM
D.
Bright Field / TMRE
TMRE / mtPAGFP
mtPAGFP
1
2
3
2 μm
E.
Mitochondrial Length
Aspect Ratio
***
CM
PDM
F.
Pre-Activation
Activation
15min post-Activation
30min post-Activation
45min post-Activation
60min post-Activation
Cytoplasmic
Peridroplet
Bright Field / TMRE
TMRE / mtPAGFP
N
10 μm
G.
Mitochondrial Fusion
PAGFP FI (% Basal)
***
*
***
***
PDM
CM
Time (min)
H.
Time = 0s
Time = 10s
Merge
Zoom
N
10 μm
6 μm
I.
Mitochondrial Motility
Displacement / time Cell Normalized
***
CM
PDM

**Figure 2.8. Peridroplet mitochondria have reduced DRP1 recruitment and OPA1 processing.**

A. Confocal image of fixed cultured brown adipocytes immunolabeled for the mitochondrial fission protein DRP1. LDs were identified by bright field images and the mitochondrial network was marked with mitochondrially-targeted DsRed (mtDsRed). Note the low levels of DRP1 recruitment to PDM (white arrows).

B. Quantification of DRP1 associated with CM and PDM. DRP1 association was quantified as puncta area divided by mitochondrial area. In each individual cell, DRP1 association to CM and PDM values were normalized to the average of the entire cell. N = 14 cells per group imaged in 3 independent experiments.

C-F. Western blot analysis of the mitochondrial inner membrane protein OPA1 in isolated PDM and CM. Proteolytic cleavage of the long-forms OPA1 (L-OPA1) to short-OPA1 (S-OPA1) is associated with inner membrane fission. Densitometry of L-OPA1 and S-OPA1 in PDM and CM are shown in representative histogram.

E-F. Quantification of total OPA1 and S-OPA1 in CM and PDM. N = 6-7 independent mitochondrial isolations.

G. Confocal images of living primary brown adipocytes transduced with DRP1-dominant negative (DRP1DN) and transduction control. LDs were identified by bright field images and the mitochondrial network was marked with TMRE.

H. Fission arrest by DRP1 dominant negative (DRP1DN) expression does not recruit mitochondria to LD surface compared to transduction control. Mitochondrial

recruitment was assessed as the area of mitochondria within 0.5 µm of LD border. N = 10 cells analyzed per group.

Data are expressed as means ± SEM. ns p> 0.05, ** p < 0.001, *** p <0.0001.

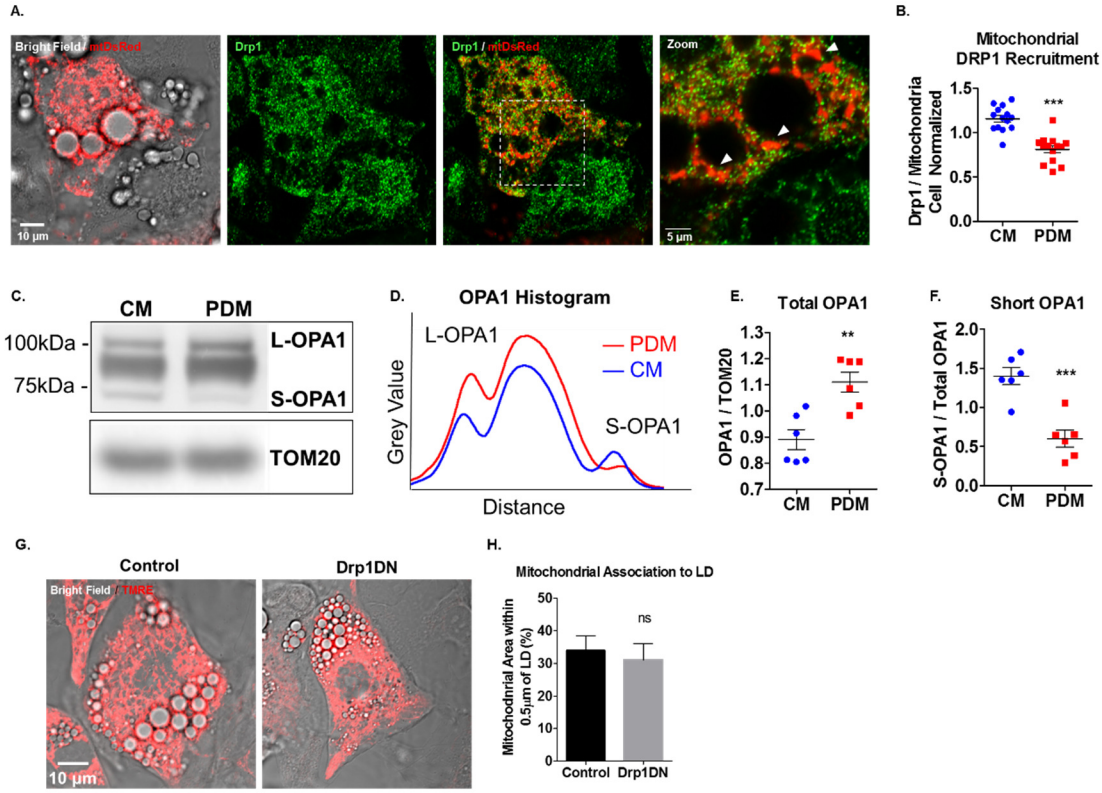

## Supplemental Figures

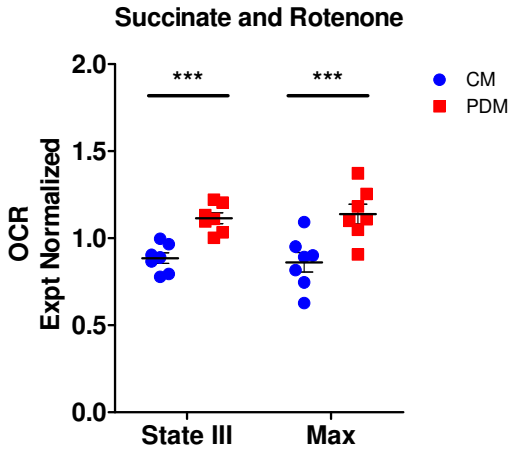


**Figure 2.1S, related to Figure 2.2.**

Quantification of respiratory states driven by succinate/rotenone in cytoplasmic (blue) and peridroplet (red) mitochondria. State III quantifies respiration driven by ATP synthesis and maximal respiration quantifies maximal electron transport activity induced by the chemical uncoupler FCCP. 6 technical replicates per group. N = 7 independent isolations. For each individual experiment, average OCR values of CM and PDM were normalized to the average OCR of all mitochondria (see Quantification and Statistical Analysis for complete equations). Data are expressed as means ± SEM. *** $p < 0.0001$.

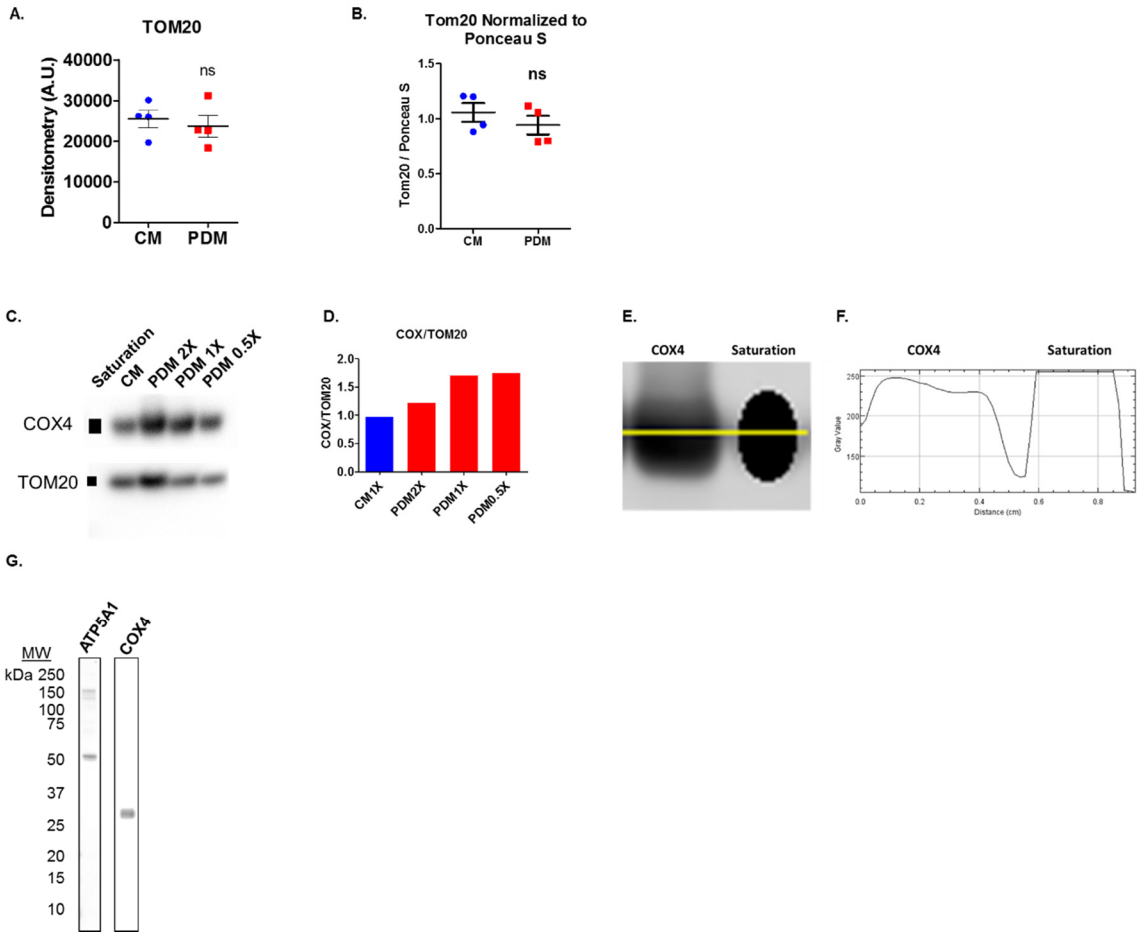


**Figure 2.2S, related to Figure 2.3.**

A. TOM20 densitometry from Western blot analysis of isolated mitochondria. N = 4 independent isolations. Experiment normalized data are expressed as means ± SEM. ns $p>0.05$.

B. TOM20 densitometry normalized to Ponceau S staining of SDS-PAGE blots of isolated mitochondria. N = 4 independent isolations. Experiment normalized data are expressed as means ± SEM. ns $p>0.05$.

C. Dilution Western blot of isolated mitochondria. One microgram of CM was compared to 2 microgram PDM (PDM 2X), 1 microgram of PDM (PDM 1X), 0.5 micrograms of PDM (0.5X), and saturating signal intensity.

D. Quantification of COX4/TOM20 ratio at different dilutions. Note that COX/Tom20 ratio is elevated in PDM independent of the amount of protein loaded.

E-F. Linescan histogram of COX4 immunostained band in isolated mitochondria subjected to western blot analysis compared to saturating signal intensity. Note that COX4 band did not exceed saturation (255 A.U. in 8-bit image).

G. Full western blot membrane of COX4 and ATP synthase antibodies used for immunofluorescence experiments. Both COX4 and ATP synthase antibodies produced robust bands at or near the predicted molecular weights (37 kDa and 53 kDA, respectively). There were moderate faint bands above 150 kDa in ATP synthase blot likely representing multimers that were not fully denatured by SDS.

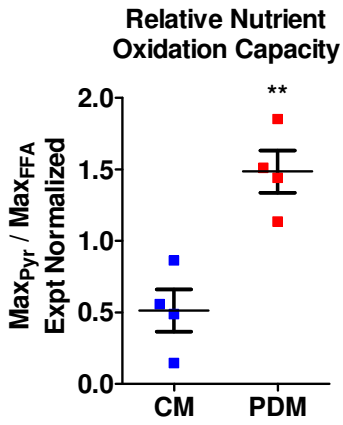


**Figure 2.3S, related to Figure 2.4.**

Maximal respiration fueled by pyruvate normalized to maximal respiration fueled by palmitoyl-carnitine ($Max_{Pyr}/Max_{PC}$) in isolated cytoplasmic (CM) and peridroplet (PDM) mitochondria. Fuels were provided to the exact same mitochondrial preparations assayed on parallels wells in same seahorse plate. N = 4 independent experiments with 4-6 technical replicates per group. Experiment normalized data are expressed as means ± SEM. ** $p < 0.001$.

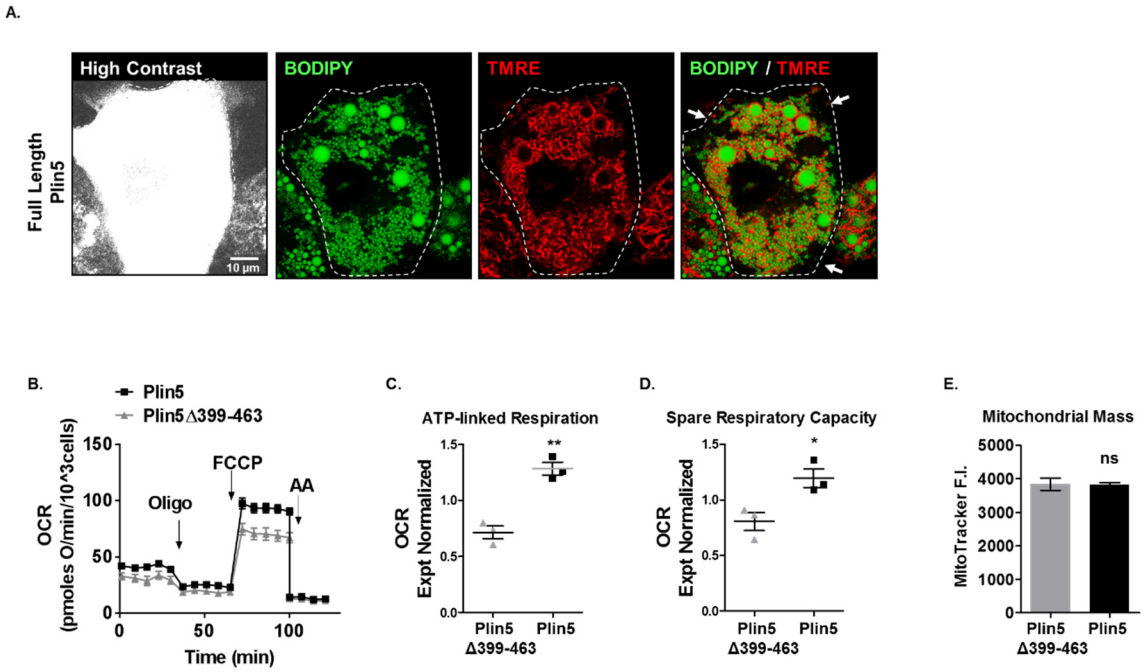


**Figure 2.4S, related to Figure 2.5.**

A. Confocal image of brown adipocyte expressing the full length Plin5, which includes mitochondrial recruiting sequence. High contrast image was used to delineate the cell borders (white striped lines). Note that there are several empty cytoplasmic spaces (white arrows).

B-D. Seahorse respirometry in cultured brown adipocytes.

B. Representative trace of oxygen consumption rate (OCR) or cultured brown adipocytes expressing full-length Plin5, which includes the mitochondrial recruiting sequence, and truncated Plin5Δ399-463, which lacks the mitochondrial recruiting sequences as a control. Oligomycin, FCCP, and Antimycin were sequentially

injected to assess ATP-linked respiration and spare respiratory capacity. 4-6 technical replicates per group. Data are expressed as means ± SEM.

C. Quantification of ATP-linked respiration in N = 3 independent experiments. Experiment normalized data are presented as means ± SEM. ** $p<0.001$,

D. Quantification of spare respiratory capacity in N = 3 independent experiments. Experiment normalized data are presented as means ± SEM. * $p<0.05$.

E. Controlling for mitochondrial mass. Quantification of mitochondrial mass in cells used for seahorse analysis by MitoTracker staining. ns $p > 0.05$.

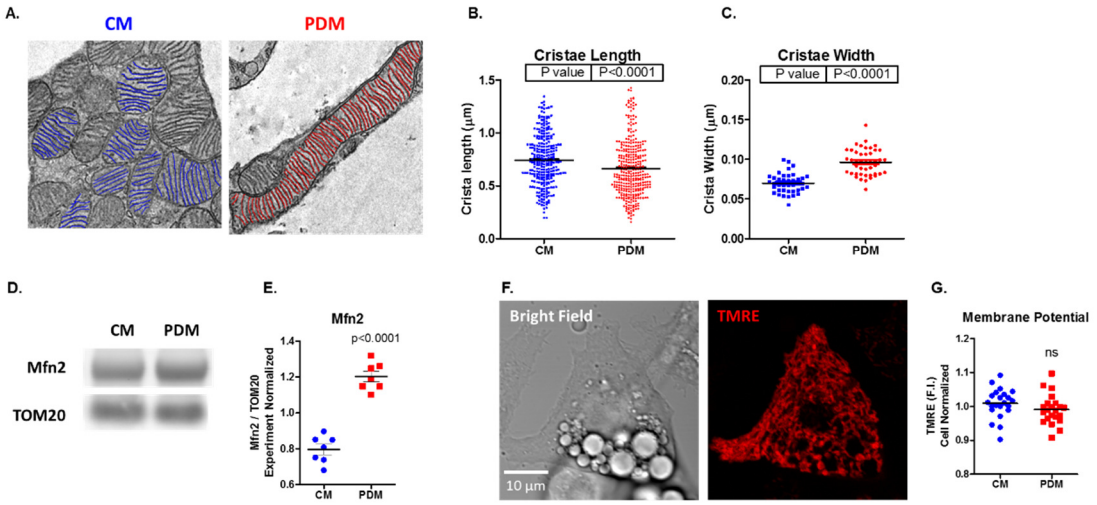


**Figure 2.5S, related to Figure 2.7.**

A-C. Cristae morphology analysis of peridroplet (PDM) and cytoplasmic (CM) mitochondria in electron micrographs of BAT harvested from mice adapted to thermoneutral environment (28°C), where PDM are most abundant. Note the uniform stacks of short thick cristae in PDM that are arranged in perpendicular orientation to the axis of mitochondria-LD interface.

D-E. Western blot analysis of Mitofusin2 (Mfn2) in isolated PDM and CM. N = 7 independent mitochondrial isolations. For each individual experiment, average values of CM and PDM were normalized to the average OCR of all mitochondria (see Quantification and Statistical Analysis for complete equations). Data are presented as means ± SEM.

F-I. Imaging of the membrane potential-sensitive dye TMRE. N = 22 cells images in 4 independent experiments. CM and PDM fluorescent intensities (F.I.) were

normalized to average cell F.I. for each individual cell. Data are presented as means ± SEM. ns $p>0.05$.

# CHAPTER THREE: Materials and Methods

## Part One: Detailed Protocol for Isolation of Lipid Droplet Bound Mitochondria from Brown Adipose Tissue

**Sample collection ●** TIMING 1-2 h

1. Dissect inter-scapular brown adipose tissue (BAT) from 6 male C57bl/6 mice and immediately place in ice-cold PBS. The number of mice needed for effective PDM isolation varies according to tissue lipid content. A minimum amount of lipid content is necessary in order to effectively collect a fat cake (see below). Fewer animals can be used if mice have higher lipid content due to age, diet, or genetic manipulation. Euthanize mice one-by-one using isofluorance or cervical decapitation protocol approved by Institutional Guidelines for Animal Care in compliance with U.S. Public Health Service Regulation. Exsanguinate mice using syringe attached to 18.5G needle prior to BAT isolation to minimize blood cell contamination.
2. Clean connective tissue, muscle, and white adipose tissue from BAT using dissection microscope.
3. Weigh pooled BAT tissue and mince into ~2mm pieces with scissors or razor. Re-suspend pieces in 10:1 volume:weight ice-cold Sucrose-HEPES-EGTA buffer supplemented with BSA (SHE+BSA; 250mM sucrose, 5mM HEPES, 2mM EGTA, 2% fatty acid-free BSA (EMD Millipore 126575), pH 7.2).

**Tissue and Cell Disruption ●** TIMING 10 min

4. Disrupt tissue with 9-10 strokes in ice-cold glass/Teflon dounce homogenizer until the liquid appears homogenous and the dounce head moves smoothly

through the tube. **CRITICAL**: all tubes and materials must be ice-cold at the beginning of the isolation and remain ice-cold throughout protocol. Do not use detergent to clean dounce homogenizer and/or cell lysis. For samples with higher content of connective tissue, use glass-glass loose dounce as an initial homogenization step.

**Separating fat cake by low-speed centrifugation** ● TIMING 20 min

5. Transfer homogenate into ice-cold 50mL falcon tube (Corning) and centrifuge 900 x g for 10 min at 4ºC in Sorvall ST 16R (thermo) with TX-200 swinging bucket rotor. **CRITICAL**: If using swigging bucket centrifuge, measure the precise distance between rotor center and the center of mass of liquid homogenate in the tube in horizontal swinging position in order to correctly calculate RPM conversion.

$$\text{rcf (g)} = 1.12 * \text{radius (mm)} * \left( \frac{\text{rpm}}{1{,}000} \right)^2$$

6. Carefully pour supernatant (Fraction 2) into a new ice-cold falcon tube so as to leave behind fat cake (Fraction 1) and debris pellet in the original tube (Figure 3.2). Keeping the original tube horizontal, scrape the Fraction 1 into a second ice-cold falcon tube and re-suspended in SHE+BSA buffer. Discard original falcon tube containing pellet unbroken cells, nuclei, and debris. **CRITICAL**: it is critical that there is enough sample to generate a solid fat cake for this procedure.
7. Repeat this step once more to pellet residual insoluble debris. **CRITICAL**: Fractions 1 and 2 must be completely cleared of debris prior to high speed

centrifugation steps. Perform additional slow-speed centrifugation speed if necessary. If residual lipid layer is present in Fraction 2 after second slow spin, discard top 1mL phase. Alternatively, submerge a gel-loading tip under lipid layer to transfer Fraction 2 to a fresh tube.

**Separating CM and PDM by high-speed centrifugation** ● TIMING 1.5 h

8. Transfer purified Fraction 1 and Fraction 2 to 2mL Eppendorf tubes and centrifuge at 10,000 x g for 10 min at 4ºC in microfuge (Thermo). Pellets will now contain peridroplet (PDM) and cytoplasmic mitochondria (CM, Figure 3.3).
9. Following centrifugation, discard the lipid layer and supernatant and gently re-suspend mitochondrial pellets in ice-cold SHE+BSA buffer: Use P1000 pipette tip to physically scrape lipid layer and gently evacuate residual lipids before removing supernatant. Once supernatant is evacuated, gently resuspend pellet in 200uL SHE+BSA and transfer all resuspended CM pellets into a single fresh ice-cold tube. Repeat with resuspended PDM pellets. **CRITICAL**: There should minimal lipid content in samples from Fraction 2. The presence of large amounts of lipid in Fraction 2 will cause CM to be contaminated by PDM. Refer to the steps above to optimize slow centrifugation steps to minimize lipid content of Fraction 2.
10. Repeat high speed centrifugation step once more with the same settings to remove residual lipids and non-mitochondrial contents.
11. Following the second high speed centrifugation, remove supernatant. There should be no visible lipid layer at this step. Perform additional centrifugation steps as needed. Gently re-suspend mitochondrial pellets in ice-cold SHE buffer

without BSA and determine protein concentration by BCA assay (Thermo). When re-suspending pellet in buffer, aim for a concentration of ~10ug/uL.

**CRITICAL**: use SHE buffer without BSA for protein determination. BSA will skew results of BCA assay.

**Respirometry** ● TIMING 1 h

12. Load Cartridge with 16.5uL MAS+ADP in Port A, 17.3uL MAS+Oligomycin in Port B, 18.5uL MAS+FCCP in Port C, 20uL MAS+AA in Port D and begin calibration in seahorse instrument.
13. Combine 2-4 ug mitochondria with 20uL MAS+PM, MAS+SR, and MAS+PC and seed each individual well in XF96 plate using P20 pipette.

    Centrifuge the plate at 2,000 x g for 5 min at 4C using plate carrier rotating buckets. **CRITICAL**: turn OFF centrifuge break and let buckets slow down independently.
14. Add 115uL MAS+GDP using multichannel pipette at a 45° angle to the top of well chamber and immediately begin run.
15. Mix Measure Delay times appear in appendix.

**Data Analysis** ● TIMING 1 h

16. Export Point-to-point oxygen consumption rates (OCRs) of individual wells from Seahorse instrument.
17. In Microsoft Excel, perform the following calculations for each individual well. Antimycin-resistant respiration is subtracted from other values to exclude non-OXPHOS OCR.

a. State II: Subtract minimal OCR value following Antimycin injection from minimal OCR value following Oligomycin injection.
b. State III: Subtract minimal OCR value following Antimycin injection from maximal OCR value following ADP injection.
c. Maximal: Subtract minimal OCR value following Antimycin injection from maximal OCR value following FCCP injection.

**Quality control** ● TIMING VARIABLE

18. To assess the quality of isolated mitochondria Option A describes measuring the lipid content of isolated mitochondria by fluorescence microscopy. Option B describes measuring relative mitochondrial protein content by biochemical techniques. Option C describes measuring mitochondrial function by membrane potential analysis.

(A) Measurement of mitochondria and LD content by fluorescence microscopy

i. Combine 1 uL of isolated mitochondria with 1uL Imaging solution A. Place 1 uL of solution on a #1.5H coverglass and cover with an additional coverglass.
ii. Place the coverglass on microscope stage and image BODIPY using 488nm laser excitation and 500-550 absorbance. Using a separate track, image MitoTracker with 633nm excitation and 650-700 absorbance. Use 20x lens for low magnification imaging of LD content.

(B) Assessment of mitochondrial content.

i. Combine 1-10 ug isolated mitochondria with protease inhibitors and boil at 95C for 5 min. Run and transfer gel as specified by gel apparatus

manufacturer. Probe for the relative content of mitochondrial markers such as Tom20 or VDAC relative to contaminant from nuclear, ER, and cytoplasmic compartments. Alternatively, evaluate mitochondrial content by mass spectroscopy proteomic analysis using MitoCarta 2.0 to estimate mitochondrial protein content.

(C) Assessment of mitochondrial function by membrane potential imaging.

i. Combine 1 uL of isolated mitochondria with 1uL Imaging solution B. Place 1 uL of solution on a #1.5H coverglass and cover with an additional coverglass.

ii. Place the coverglass on microscope stage and image MitoTracker green using 488nm laser excitation and 500-550 absorbance. Using a separate track, image MitoTracker Red with 633nm excitation and 650-700 absorbance.

iii. Mitotracker Red is sensitive to real time changes in membrane potential while MitoTracker Green is not sensitive, as it is a cumulative mitochondrial protein dye. Therefore, functional mitochondria will stain with both Green and Red while mitochondria with reduced membrane potential will only stain green.

## Figures

**Figure 3.1. Schematic representation of peridroplet mitochondrial (PDM) isolation procedure.**

Interscapular brown adipose tissue (BAT) was dissected from mice and homogenized with glass-Teflon dounce homogenizer. Low-speed centrifugation separated fat cake containing PDM from supernatant containing cytoplasmic mitochondria (CM). High-speed centrifugation stripped PDM from lipid droplets (LDs) and pelleted CM mitochondria from the supernatant. Note that some BAT mitochondrial isolation protocols discard the fat cake and/or begin with high-speed centrifugation step.

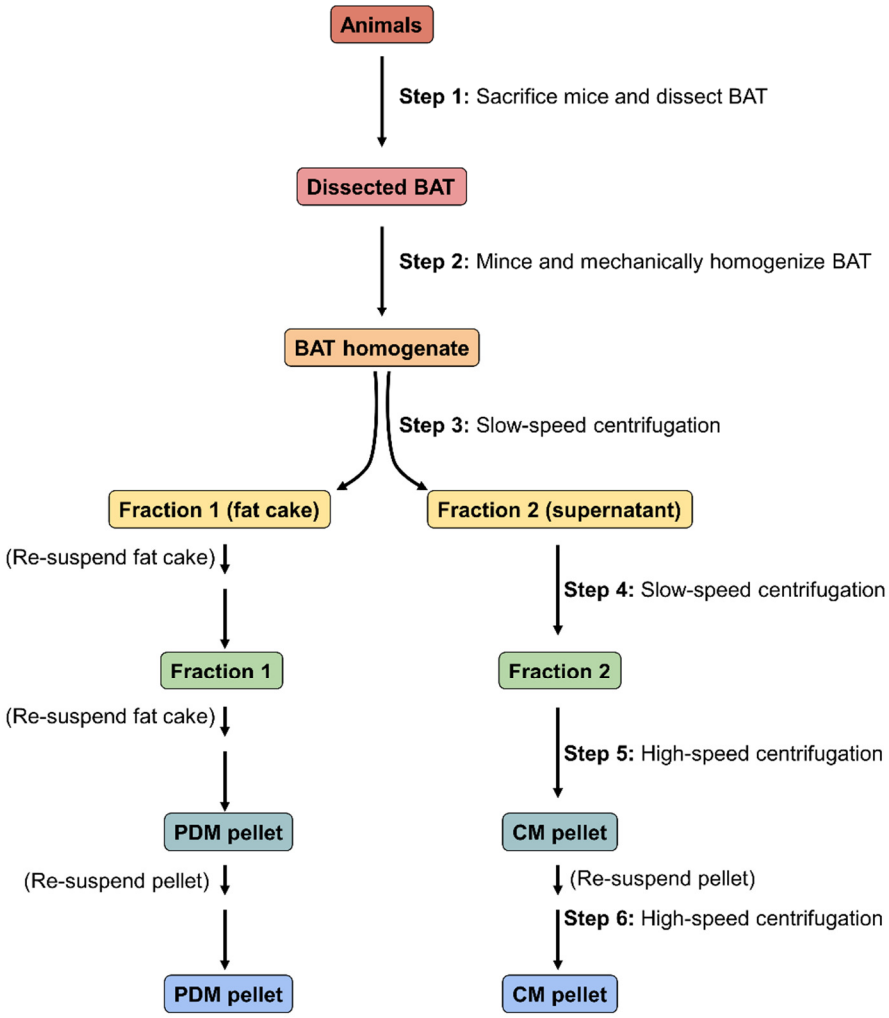
Animals
Step 1: Sacrifice mice and dissect BAT
Dissected BAT
Step 2: Mince and mechanically homogenize BAT
BAT homogenate
Step 3: Slow-speed centrifugation
Fraction 1 (fat cake)
Fraction 2 (supernatant)
(Re-suspend fat cake)
Step 4: Slow-speed centrifugation
Fraction 1
Fraction 2
(Re-suspend fat cake)
Step 5: High-speed centrifugation
PDM pellet
CM pellet
(Re-suspend pellet)
(Re-suspend pellet)
Step 6: High-speed centrifugation
PDM pellet
CM pellet

**Figure 3.2. Separation of fractions by slow-speed centrifugation.**

A. Image of 50mL falcon tube containing BAT homogenate after first slow speed centrifugation (Step 3). Note the separation of Fraction 1 and 2. B-C. Supernatant was carefully poured into a fresh ice-cold 50mL falcon tube so as to keep fat cake in the original falcon tube. The decanted original tube (B) was placed horizontally on ice to harvest fat cake.

A.

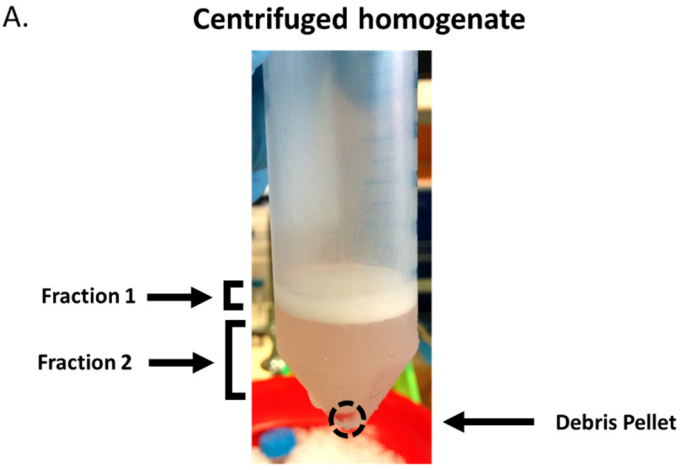
Centrifuged homogenate
Fraction 1
Fraction 2
Debris Pellet

B.

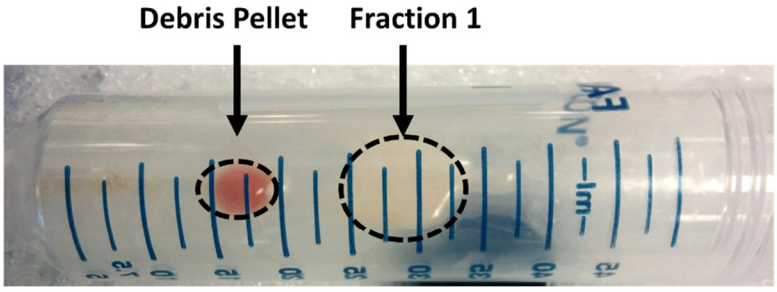
Debris Pellet
Fraction 1

C.

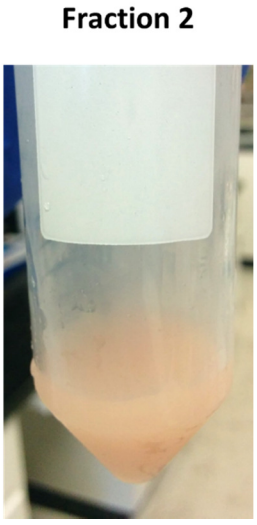
Fraction 2

**Figure 3.3. Mitochondrial isolation by high-speed centrifugation.**

A. Re-suspended Fraction 1 and Fraction 2 before high-speed centrifugation. B. Top and side views of Fraction 1 and Fraction 2 after high-speed centrifugation. Note that Fraction 2 should have minimal fat layer compared to Fraction 1. Perform additional slow centrifugations steps if Fraction 2 has high lipid levels. See text for details.

A.

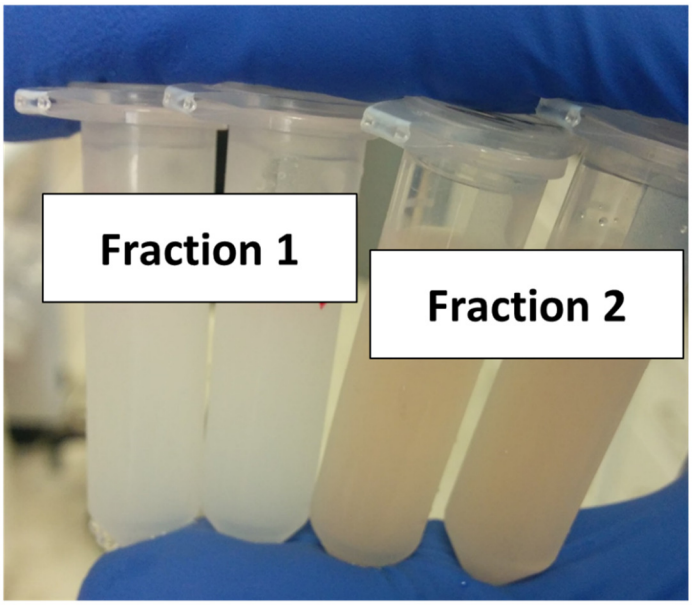
Fraction 1
Fraction 2

B.

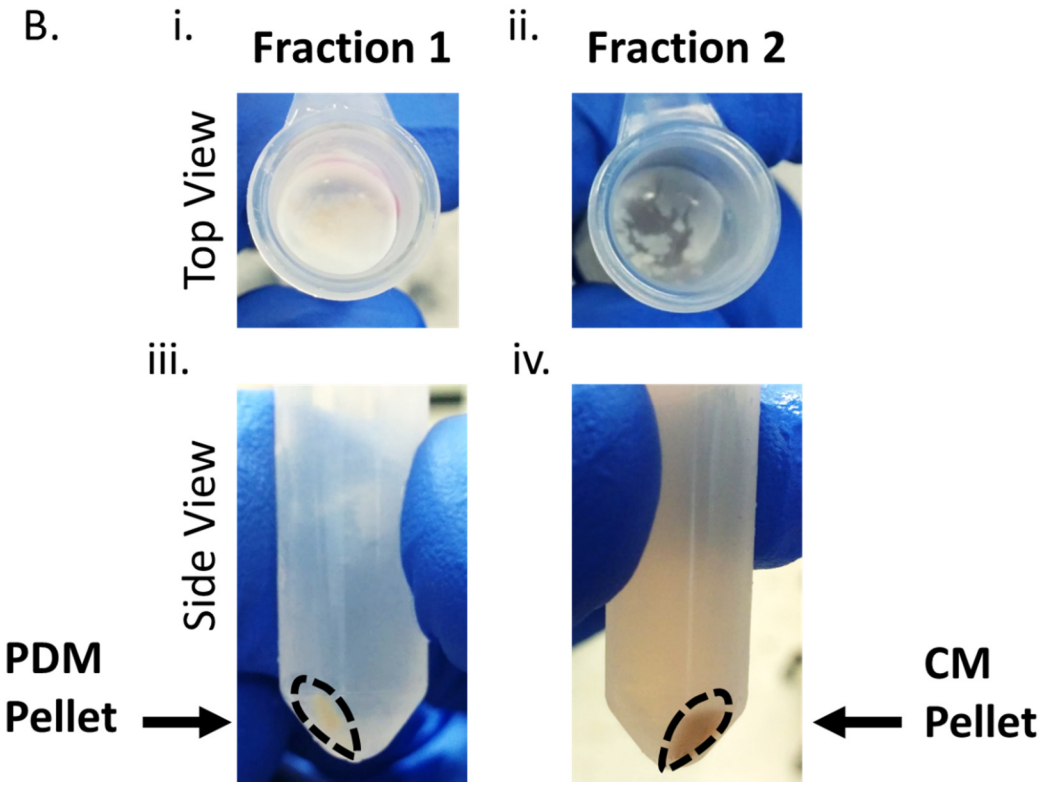
i.
Fraction 1
ii.
Fraction 2
Top View
iii.
iv.
Side View
PDM
Pellet
CM
Pellet

## Part Two: Materials and Methods

### Experimental Models and Subjects Details

Mitochondria were isolated from 12-week-old male C57BL6/J mice and primary brown adipocytes were isolated from 3 to 4-week-old wild-type male C57BL6/J mice (Jackson lab, Bar Harbor, ME). Animals were fed standard chow (mouse diet 9F, PMI Nutrition International, Brentwood, MO) and maintained under controlled conditions (19–22°C and a 14:10 h light-dark cycle) until euthanasia by isoflurane. All animal procedures were performed in accordance with the Guide for Care and Use of Laboratory Animals of the NIH, and were approved by the Animal Subjects Committee of the University of California, Los Angeles, and the Boston University Institutional Guidelines for Animal Care.

### Cell Culture

Primary brown adipocytes isolation and culture: Brown adipose cells were isolated and cultured as described in (Cannon and Nedergaard, 2001b). BAT was dissected from interscapular, subscapular, and cervical regions of three male mice, minced, and transferred to 10mL collagenase digestion buffer in 50mL Falcon tube (2mg/mL Collagenase Type II in 100 mM HEPES, 120 mM NaCl, 4.8 mM KCl, 1mM CaCl2, 4.5 mM Glucose, 1.5% BSA, pH 7.4). Collagenase digestion was performed in 37°C water incubator under constant agitation for 25 minutes with vortex agitation every 5 min. Digested tissue was homogenized with 18.5G needle and strained through 100 µm and 40 µm filters. 30mL of ice-cold DMEM was added

to tissue digest and centrifuged at 200 x g for 10 minutes at 4°C in Sorvall ST 16R (Thermo) with TX-200 swinging bucket rotor. Media was carefully removed and the cell pellet re-suspended in 30mL ice-cold DMEM media. Cells were centrifuged again with the same settings. Next, the cell pellet was re-suspended 5mL growth medium (DMEM supplemented with 10% newborn calf serum (NCS), 4 mM Glutamine, 10 mM HEPES, 0.1mg/mL sodium ascorbate, 50 U/ml penicillin, 50 µg/mL streptomycin) and plated in 6-well plate (Corning). Cells were incubated in 37°C 8% CO2 incubator. 48 Hours are after isolation, the cells were washed to remove debris and media was replaced. 72 hours after isolation the cells were lifted using STEMPro Accutase, counted, and re-plated in differentiation media (growth media supplemented with 1 µM rosiglitazone maleate and 4 nM porcine insulin) in final experimental vessel. Cells were differentiated for 7 days and media was changed every other day. For transduction experiments, cells were transduced with virus in differentiation day 0-3.

Brown adipocyte immortalization: Brown preadipocytes immortalized by SV40T antigen were kindly provided by Drs. Pedro Quiros and Carlos Lopez-Otin (Quirós et al., 2012). Immortalized preadipocytes were differentiated for 7 days in culture medium supplemented with 20 nM insulin and 1 nM T3, 0.5 mM isobutylmethylxanthine, 0.5 µM dexamethasone, and 0.125 mM indomethacin (Fasshauer et al., 2000) in 37°C 5% CO2 incubator.

INS1 culture: INS-1 832/13 cells were cultured in RPMI 1640 medium supplemented with 10% fetal calf serum (FBS), 10 mM HEPES buffer, 1 mM pyruvate, 50 µM 2-ß-mercaptoethanol, 50 U/ml penicillin and 50 µg/ml streptomycin. Cells were incubated in 37°C 5% CO2 incubator and used between passage 60 and 80.

**Peridroplet mitochondrial isolation**

All procedures were performed using pre-chilled equipment and solutions. Interscapular BAT from 6 mice was harvested and rinsed in PBS. Tissue was weighed, minced, and suspended in 6 mL (~1mL/100mg tissue) Sucrose-HEPES-EGTA buffer supplemented with BSA (SHE+BSA; 250 mM sucrose, 5 mM HEPES, 2 mM EGTA, 2% fatty acid-free BSA, pH 7.2). The preparation was then mechanically homogenized with 9 strokes in glass-teflon dounce homogenizer. The homogenate was then transferred to 50mL falcon tube (Corning) and centrifuged in Sorvall ST 16R (Thermo) with TX-200 swinging bucket rotor at 900 x g for 10 min at 4°C. Supernatant was carefully poured into a new ice-cold falcon tube so as to leave the fat layer in the original tube. Keeping the original tube horizontal, the fat layer was scraped into a second ice-cold falcon tube and re-suspended in SHE+BSA buffer. The two fractions were centrifuged again at 900 x g for 10 min at 4°C and then transferred into 2mL Eppendorf tubes and centrifuged in a microcentrifuge (Thermo) at 9,000 x g for 10 min at 4°C. The pellets were resuspended in SHE+BSA and centrifuged with the same settings once more. The

pellets were then re-suspended in SHE without BSA and protein concentration was determined by BCA (Thermo). BSA was omitted from the final isolation buffer to prevent interference with BCA assay.

**Fluorescence microscopy**

Imaging apparatus: All imaging was performed on Zeiss LSM710 and LSM880. Super-resolution imaging was performed with 63x Apochromat oil-immersion lens and AiryScan super-resolution detector (Huff, Bathe, Netz, Anhut, & Weisshart, 2015). Low-resolution images were captured with 10x air objective. Live cell imaging was performed with humidified 5% $CO_2$ chamber on a temperature controlled stage at 37°C.

Fluorophore excitation/emission: All fluorophores were excited on separate tracks to avoid artifacts due to bleed-through emission. DAPI was excited with 405nm 30mW laser and its emission captured through 485nm short-pass filter. BODIPY 493/503, Alexa-Fluor 488, MitoTracker green, and PAGFP were excited with 488nm 25mW Argon-ion laser and their emission captured through 500-550nm band-pass filter. Alexa-Fluor 546, TMRE, and mtDsRed were excited with 543nm 1mW Helium-Neon laser or 561nm 20mW diode-pumped solid-state laser and their emission captured through a 580-650nm band-pass filter. MitoTracker deep red was excited using 633nm 5mW Helium-Neon laser and its emission captured through a 645nm long-pass filter.

Fat layer and isolated mitochondria: 1µL of re-suspended preparation was combined with 1µL SHE buffer supplemented with 1µM MitoTracker deep red and 1µM BODIPY 493/503 on a 1.0mm glass slide (EMS 71867) and covered with #1.5 thickness coverglass (EMS 72222). Imaging was performed using 63x Apochromat oil-immersion lens.

Live cells: Cells were seeded, transduced, and differentiated in glass-bottom confocal plates (MatTek P35G-0.170-14-C). On the day of the experiment, DAPI was loaded at 1µg/mL, BODIPY 493/503 was loaded at 200 nM and TMRE was loaded at 15 nM for 90 min followed by BODIPY wash-out before imaging. DAPI and BODIPY were washed out while TMRE was present during imaging.

Image analysis: All image analysis was performed in FIJI (ImageJ, NIH). Individual mitochondrial fluorescence intensity and area were measured in FIJI and imported into Microsoft Excel. Mitochondria smaller than 10 pixels in area were not included in final analyses. Mitochondria within 0.5 µm of lipid droplet edge were defined as PDM while mitochondria beyond 0.5 µm peridroplet region were defined as CM.

Step-by-step instructions:

1. Manually circle LDs in bright-field image using Oval tool or threshold in BODIPY 493/503 image using Image>Adjust>Threshold (keyboard shortcut: "CNTRL+Shift+T"). Add LD regions to ROI manager (Edit>Selection>Add to manager; keyboard shortcut: “T”). ROI manager can be opened from here: Analyze>Tools>ROI Manager.

2. When selection of LDs is completed, Highlight all LDs in ROI manager by clicking “CNTRL+A”. Click "More>>" button and select "OR". This will combine all ROIs into a single ROI. Press the key "T" to add newly modified ROI to ROI manager. Select this region in ROI manager and Rename it “LD ROI”. Click "More>Save" to save ROI.

3. Enlarge LD mask by 0.5 microns by clicking Edit>Selection>Enlarge and entering the value "0.5". Press "T" to add newly modified ROI to ROI manager. Select this region in ROI manager and Rename it “Enlarged LD ROI”. Click "More>Save" to save ROI. ***CRITICAL: make sure image scale is correct. For example, a high resolution image captured with 63x objective is ~ 50x50 micrometers and 1400x1400 pixels, resulting in 28 pixels per micron. You can check image scale in Analyze>Set Scale.

4. Open TOM20 or matrix-targeted DsRed image and threshold using Image>Adjust>Threshold (keyboard shortcut: "CNTRL+Shift+T"). Select the most suitable thresholding algorithm to highlight all mitochondria from drop-down menu. Once mitochondria are highlighted, select Edit>Selection>Create Selection.

5. Press "T" to add to ROI manager. Select this region in ROI manager and Rename it “Total mitochondria ROI”. Click "More>Save" to save mask.

6. Highlight Enlarged LD ROI and Total mitochondrial ROI in ROI manager and click “More>AND”. This will combine pixels present in both regions into a single

region. Select this region and rename it “PDM ROI”. Click "More>Save" to save mask.

7. Highlight Enlarged LD ROI and Total mitochondrial ROI in ROI manager and click “More>XOR”. This will exclude PDM region. Select this region and rename it “CM ROI”.

8. Open COX4 image. Select PDM ROI from ROI manager. Select “More>Split” to split ROI into individual mitochondrial regions. Measure by clicking "Analyze>Measure" or clicking the "M" key. This will open the Results dialogue box. If Results dialogue does not contain desired columns, click the following checkboxes in Analyze>Set Measurements: "Area" will display the area of ROI in microns; "Integrated density" will display the sum of pixel intensity values in ROI; "Mean Gray value" will display the average pixel intensity value in ROI; "Display Label" will display ROI next before each row of data.

9. Select CM mask from ROI manager. Select “More>Split” to split ROI into individual mitochondrial regions. Click "M" key to measure.

10. In Excel, record Mean gray value for CM and PDM. Exclude mitochondria that are smaller than 10 pixels in area.

Image presentation: Image contrast and brightness were not altered in any quantitative image analysis protocols. Brightness and contrast were optimized to properly display representative images in figure panels. Display settings are equivalent in images directly compared to one another.

**Isolated Mitochondria Proteomics**

100 micrograms of isolated mitochondria were re-suspended in 6M Urea 100 mM Tris, pH 8.5 and then reduced and alkylated by incubation in 5 mM TCEP-HCL for 20 min at room temperature, in the dark (Langousis et al., 2016). Lys-C was introduced to the protein suspension at an enzyme to substrate ratio of 1:100, and incubated for 4 hours at 37°C. Samples were subsequently diluted to 2M Urea by addition of 100 mM Tris, pH 8.5. A final concentration of 1 mM $CaCl_2$ was added to the solution, and Trypsin introduced at an enzyme to substrate ratio of 1:50 overnight at 37°C. Proteolytic digestion was quenched by the addition of formic acid to a final concentration of 5%. Prior to mass spectrometric analysis, samples were desalted on Pierce C18 StageTips and eluted in 40% ACN before vacuum drying and resuspension in 5% formic acid. Desalted samples were separated on a 100µM internal diameter, revered phase fused silica column packed with 18cm of 1.9 µM C18 particles (Dr. Maisch, GmbH) with an integrated 5µM pulled electrospray emitter. Gradient delivery as performed on an Easy nLC-1000 UHPLC at 300 nl/min, and MS/MS spectra generated by Data Dependent Acquisition on a Thermo Q-Exactive mass spectrometer. Data analysis was carried out using the Integrated Proteomics pipeline 2 (Integrated Proteomics Applications, Inc., San Diego, CA). Specifically, MS/MS spectra were searched with the ProLuCID algorithm, and PSM confidence was estimated by DTASelect. Search was performed against the Uniprot Mouse proteome containing only

reviewed proteins, downloaded on 08/29/2016. Peptide spectrum identifications were filtered at a 1% maximum false detection rate as estimated by a target-decoy database search strategy. Protein identifications were only considered after reaching the requirement of a minimum of two confidently identified peptides. The IP2 pipeline provided normalized spectral abundance factor and spectral count calculations for set comparisons.

**Isolated Mitochondria Respirometry**

Isolated mitochondria were re-suspended in respiration buffer (100 mM KCl, 10 mM $KH_2PO_4$, 2 mM $MgCl_2$, 5 mM HEPES, 1 mM EGTA, 0.1% BSA, 1 mM GDP, pH 7.2) containing substrates (Mahdaviani et al., 2017). Four micrograms per well were loaded into Seahorse XF96 microplate in 20µL volume. The loaded plate was centrifuged at 2,000 x g for 5 min at 4°C and an additional 115 µL of buffer+substrate was added to each well. Substrate concentrations were as follow: 5 mM Pyruvate + 5 mM Malate, 5mM Succinate + 2 µM Rotenone, 40 µM palmitoyl-Carnitine + 1 mM Malate. ADP was injected at port A (3.5 mM final concentration), 20 Oligomycin at port B (3.5 µM), FCCP at port C (4 µM) and Antimycin A at port D (4 µM). Mix and measure times were 0.5 minutes and 4 minutes, respectively. A 2 minute wait time was included for oligomycin-resistant respiration measurements.

**Cytochrome c oxidase TMPD/Ascorbate respirometry assay**

Isolated mitochondria were re-suspended in ice-cold respiration buffer and kept on ice. Two micrograms of isolated mitochondria were re-suspended in respiration buffer and plated on a seahorse XF96 microplate 20 µL volume. Cytochrome c oxidase activity was exclusively assessed using 100 µM N,N,N',N'-Tetramethyl-p-phenylenediamine (TMPD) and 10 mM Ascorbate, as previously described in detail (Divakaruni et al., 2014). To exclude respiration mediated by TCA and other electron transport complexes, we injected antimycin/rotenone injection at the start of the assay. We confirmed that cytochrome c was not a limiting factor as supplementing assay media with exogenous cytochrome c did not alter TMPD/ascorbate-mediated respiration. We injected the COX-specific inhibitor sodium azide at the end of the assay to confirm that TMPD/ascorbate-driven respiration was specific to COX activity.

**ATP Synthesis Assay**

One microgram of isolated mitochondria were re-suspended in mitochondrial respiration buffer containing 5 mM pyruvate + 5 mM malate + 3.5 mM ADP and kept on ice (Wibom, Lundin, & Hultman, 1990). 50 µL of this mixture was combined with 50 µL of Luciferin-luciferase mix in clear-bottom black 96-well plate (Corning) and measured immediately. We determined the optimal concentration of reagents and measurement settings on our instrument using HPLC-purified ATP standards. Luminescent counts were integrated over 0.5 seconds at 10 second intervals separated by 0.5 second orbital shaking on Spark M10 microplate reader (Tecan).

To control for non-OXPHOS ATP synthesis, we assessed luminescence in parallel samples that were treated with the ATP synthase inhibitor oligomycin A. We confirmed ATP contamination of ADP preparation was minimal by assaying ADP by itself. The linear rate of luminescence increase was calculated to determine ATP synthesis rate.

**Protein Gel Electrophoresis and Immunoblotting**

SDS-PAGE: 10-20 µg of isolated mitochondrial protein was re-suspended in NuPAGE LDS Sample Buffer with protease inhibitor cocktail and incubated at 45C for 10 min. Samples were then loaded into 4-12% Bis-Tris precast gels (ThermoFisher Sci. NP0321) and electrophoresed in xCell SureLock (Novex) in constant voltage at 60V for 15 minutes (to clear stacking) and 150V for 45 minutes. Blue native gel electrophoresis: 10-50 µg of isolated mitochondrial protein was re-suspended in 20 µL solubilization buffer (50mM Imidazole, 500mM 6-aminohexanoic acid, EDTA 1mM pH 7.0)(Wittig, Braun, & Schägger, 2006). 8 mg digitonin/mg of mitochondrial protein was added and samples were incubated on ice for 5 minutes. Since commercial digitonin is only 50% pure, we used 16 mg of crude powder to achieve 8mg (no re-crystallization). Digitonin was dissolved in PBS by boiling and stored at 4°C until use. Solubilized samples were centrifuged at maximal speed in a microcentrifuge (Thermo) for 30 min at 4°C. Pellet was discarded and supernatant was combined with 1 µL of 2.5% Coomassie G-250. Samples were loaded into NativePAGE 3-12% Bis-Tris gel and electrophoresed

at 4°C in xCell SureLock (Novex) in constant voltage at 20V for 60 minutes and 200V for 120 minutes or until dye front exited the gel.

Immunoblotting: Proteins were transferred to methanol-activated PVDF membrane in xCell SureLock in 30V constant voltage for 1 hour at 4°C. Commassie was completely washed off blue native blots using 100% methanol. Blots were blocked with 5g/100mL non-fat dry milk in 0.5ml/L PBST (1mL/L Tween-20/PBS) and incubated with primary antibody diluted in 1g/100mL BSA/PBST overnight at 4°C. The next day, blots were washed 3x10min in PBST, probed with HRP-linked secondary antibodies diluted in blocking solution for 1 hour at room temperature, and rinsed again 3x10min in PBST. Detection was achieved by ECL-Plus reagent and imaging was performed with Typhoon 9410 Molecular Imager (Amersham). Image contrast was uniformly reduced to enhance visibility. Band densitometry was quantified using ImageJ Gel Plugin (NIH).

**Immunofluorescence**

Cells were cultured, transduced, and differentiated on coverslips and fixed at 4% vol/vol PFA for 15 min at room temperature. After washing in PBS, cells were incubated in permeabilization buffer (2 µl/mL Triton X-100, 0.5 mg/mL Sodium Deoxycholate in PBS, pH 7.4) for 15 min at room temperature. Cells were then blocked with 3g/100mL BSA for 1 hour at room temperature. Next, cells were incubated with 1:200 primary antibody at 4°C overnight. The next day, cells were washed in PBS and incubated with 1:500 Anti-Mouse Alexa Fluor 488 or Anti-

Mouse Alexa Fluor 546 secondary antibodies for 1 hour at room temperature. After washing in PBS, coverslips were mounted in MOWIOL on glass slide, air-dried, and stored at 4°C.

**Citrate Synthase Assay**

Citrate synthase activity was performed using 5,5′-Dithiobis(2-nitrobenzoic acid) (DTNB) (Spinazzi, Casarin, Pertegato, Salviati, & Angelini, 2012). Isolated mitochondria were re-suspended in 200mM Tris buffer containing 0.2% v/v Triton X-100 (pH 8.0), 100 µM DTNB, and 300 µM acetyl-CoA and loaded into a clear-bottom black 96-well plate. Baseline 412nm absorbance was measured using Spark M10 microplate reader (Tecan). Oxaloacetate was then added and 412nm absorbance was repeatedly measured at 20 second intervals. The linear rate of absorbance increase was calculated to determine citrate synthesis rate.

**NAD(P)H Imaging**

NAD(P)H autofluorescence was excited using 730nm 2-photon Chameleon Vision laser (Coherent) to give 365 nm photo-equivalence at the focal plane. 425-475nm emission was detected by ultra-high sensitivity Gallium Arsenide Phosphide detectors with non-descanned beampath to maximize emission collection and minimize laser power. To minimize artifacts due to phototoxicity and bleaching, image acquisition settings were optimized on a test cell that was not included in final image analysis. Images of analyzed cells were subsequently acquired using a single laser scan.

**Electron Microscopy**

Interscapular brown adipose tissue was harvested from mice acclimated to 28°C for 2-4 weeks and from mice acclimated to 6°C for 1-5 days. Small tissue fragments were fixed in 2% glutaraldehyde/2% paraformaldehyde in 0.1M phosphate buffer, pH 7.4, for 4 hours at room temperature (Cinti et al., 2002). Samples were post-fixed in 1% osmium tetroxide, dehydrated in ethanol, and embedded in epoxy resin. Thin sections were obtained by MTX ultramicrotome (RMC, Tucson, AZ), stained with lead citrate, and imaged with Philips CM10 transmission electron microscope (Philips, Eindhoven, Netherlands). Imaging of cross-ruled grating of known distance was used to calibrate images.

Image analysis: Mitochondria were manually traced in electron micrographs and quantified in ImageJ. Aspect ratio was calculated as the major axis divided by the minor axis.

**Virus Preparation**

Plin5 and Plin5Δ399-463 constructs were a generous gift from Carole Sztalyrd (H. Wang et al., 2011). Plasmids were modified to express mKATE2 far-red fluorophore to enhance compatibility with fluorescent dyes and packaged into adenoviral particles (Welgen, Inc.). Viral transduction was confirmed by mKATE2 fluorescence. Lentiviral particles for mtPAGFP, mtDsRed, and DRP1DN were generated as previously described in detail (Wikstrom et al., 2014).

Gene delivery: Pre-adipocytes and INS1 cells were incubated with 0.3 µL/mL of adenoviral preparation for 5 hours in complete culture media. This was sufficient to achieve transduction in the majority of cells with little to no toxicity as assessed by cell division and viability. Fluorescent label and protein expression were detectable at differentiation day 7. Lentiviruses were delivered as previously described in detail (Wikstrom et al., 2014).

**Lipolysis Assay**

Cells were seeded, transduced and differentiated in 96-well plate. On the day of experiment, the cells were washed once and incubated with 100 µL Krebs-Ringer Bicarbonate Buffer (KRB; 119mM NaCl, 4.6mM KCl, 5mM NaHCO3, 2mM CaCl2, 1mM MgSO4, 0.15mM Na2HOP4, 0.4mM KH2PO4, 20mM HEPES, 5mM Glucose, pH 7.4) for 2 hours. KRB was collected and assayed for glycerol using Free Glycerol Colorimetric/Fluorometric Assay Kit (BioVision) according to the manufacturer instructions.

**Thin Layer Chromatography**

Cells were seeded, transduced, and differentiated in 6-well plate. Cells were washed and incubated with overnight with 1 µM BODIPY C12 558/568 as previously described (Rambold et al., 2015). Cells were harvested using Accutase and spun down. Cellular lipids were extracted in chloroform and developed on aluminum-backed silica plates (Sigma 55811) using 1:2 cyclohexane:ethyl

acetate. Plates were imaged using Typhoon 9410 Molecular Imager (Amersham) and spots were quantified using ImageJ Gel Plugin.

**Mitochondrial Fusion Assay**

Brown adipocytes were seeded, transduced, and differentiated in glass-bottom confocal plates (MatTek). mtPAGFP was activated using 750nm 2-photon Chameleon Vision laser (Coherent) to give 375nm photo-equivalence at the focal plane (Twig et al., 2008, 2010). The diffusion of mtPAGFP was assessed by repeatedly scanning the cell at 15 minute intervals. GFP fluorescence was quantified within the region of interest at every time point to assess diffusion. Diffusion of cytosolic mitochondria PAGFP reached as steady state within 40-50 minutes after photo-activation. At this time point, mitochondria that retained non-diluted GFP were defined as non-fusing mitochondria.

**QUANTIFICATION AND STATISTICAL ANALYSIS**

All data analyses were performed using GraphPad Prism 5 and Microsoft Excel. Raw data from each individual experiment was evaluated using an unpaired two-tailed t-test with 95% confidence in Prism. For data sets that did not pass the D'Agostino and Pearson omnibus normality test (alpha = 0.05), differences were evaluated using a two-tailed unpaired non-parametric Mann-Whitney test with 95% confidence. For repeated independent experiments, the raw data of CM and PDM from each individual experiment were normalized to the average value of all mitochondria in that specific experiment as shown in the formula below.

Experiment-normalized data was then evaluated by a paired two-tailed t-test with 95% confidence.

$$\mathrm{CM}_{\mathrm{normalized}} = \frac{\sum \mathrm{CM}_{\mathrm{raw\ values}} \Big/ \text{number of CM replicates}}{\left(\sum \mathrm{CM}_{\mathrm{raw\ values}} + \sum \mathrm{PDM}_{\mathrm{raw\ values}}\right) \Big/ \text{total number of CM and PDM replicates}}$$

$$\mathrm{PDM}_{\mathrm{normalized}} = \frac{\sum \mathrm{PDM}_{\mathrm{raw\ values}} \Big/ \text{number of PDM replicates}}{\left(\sum \mathrm{CM}_{\mathrm{raw\ values}} + \sum \mathrm{PDM}_{\mathrm{raw\ values}}\right) \Big/ \text{total number of CM and PDM replicates}}$$

**Key resource table**

| REAGENT or RESOURCE | SOURCE | IDENTIFIER |
|---|---|---|
| Antibodies | | |
| Mouse anti-Complex I NDUFB8 | ThermoFisher Sci. | Clone 20E9DH10C12, Cat. #459210 |
| Mouse anti-Complex II SDHB | Abcam | Clone EPR10880, Cat. #175225 |
| Mouse anti-Complex III UQCRC1 | ThermoFisher Sci. | Cone 16D10AD9AH5, Cat. #459140 |
| Mouse anti-Complex 4 COX4 | ThermoFisher Sci. | Clone 1D6E1A8, Cat. #459600 |
| Mouse anti-ATP Synthase ATP5A1 | ThermoFisher Sci. | Clone 15H4C4, Cat. #43-9800 |
| Rabbit anti-TOM20 | Santa Cruz Biotech. | Cat. #11415 |
| Rabbit anti-UCP1 | Abcam | Cat. #10983 |
| Mouse anti-DLP1 (DRP1) | BD Biosciences | Clone 8/DLP1, Cat. #611113 |
| Mouse anti-OPA1 | BD Biosciences | Clone 18/OPA1, Cat. #612607 |
| Anti-mouse HRP-linked | Cell Signaling Tech. | Cat. #7076S |
| Anti-rabbit HRP-linked | Cell Signaling Tech. | Cat. #7074S |
| Goat anti-Mouse IgG (H+L) Secondary Antibody, Alexa Fluor 488 conjugate | ThermoFisher Sci. | Cat. #A11001 |
| Donkey anti-Rabbit IgG (H+L) Secondary Antibody, Alexa Fluor 546 conjugate | ThermoFisher Sci. | Cat. #A10040 |
| Bacterial and Virus Strains | | |
| Full-length Plin5 Adenovirus that includes mitochondrial recruiting sequence | Welgen, Inc. | Ad-CMV- Plin5(aa1-463)-mKate2 |
| Truncated Plin5Δ399-463 Adenovirus lacking mitochondrial recruiting sequence | Welgen, Inc. | Ad-CMV- Plin5(aa1-399)-mKate2 |
| mt-PAGFP Lentivirus | (Twig et al., 2008) | pLV-CATG Trono Lab/Addgene |
| mt-DsRed Lentivirus | (Twig et al., 2008) | pLV-CATG Trono Lab/Addgene |

| Biological Samples | | |
|---|---|---|
| Interscapular brown adipose tissue from healthy 12-week-old male C57BL/6J | Jackson lab | Cat. #000664 |
| Chemicals, Peptides, and Recombinant Proteins | | |
| Fatty Acid-Free Bovine Serum Albumin | EMD Millipore | Cat. #126575 |
| BODIPY 493/503 (4,4-Difluoro-1,3,5,7,8-Pentamethyl-4-Bora-3a,4a-Diaza-s-Indacene) | ThermoFisher Sci. | Cat. #D3922 |
| MitoTracker Deep Red FM | ThermoFisher Sci. | Cat. #M22426 |
| MitoTracker Green FM | ThermoFisher Sci. | Cat. #M7514 |
| Tetramethylrhodamine, Ethyl Ester, Perchlorate (TMRE) | ThermoFisher Sci. | Cat. #T669 |
| Ultrapure dimethyl sulfoxide (DMSO) | Amresco | Cat. #N182 |
| Sodium Pyruvate | ThermoFisher Sci. | Cat. #BP356 |
| L-(-)-Malic Acid | Sigma-Aldrich | Cat. #M6413 |
| Succinic Acid | Sigma-Aldrich | Cat. #S9512 |
| Rotenone | Sigma-Aldrich | Cat. #R8875 |
| Palmitoyl-L-carnitine chloride | Sigma-Aldrich | Cat. #P1645 |
| Adenosine 5'-diphosphate monopotassium ADP) | Sigma-Aldrich | Cat. #A5285 |
| Oligomycin A | Sigma-Aldrich | Cat. #75351 |
| FCCP | Sigma-Aldrich | Cat. #C2920 |
| Antimycin A | Sigma-Aldrich | Cat. #A8674 |
| N N N' N'-tetramethyl-p-phenylenediamine (TMPD) | Sigma-Aldrich | Cat. #T7394 |
| (+)-Sodium L-Ascorbate | Sigma-Aldrich | Cat. #A4034 |
| Sodium Azide | Sigma-Aldrich | Cat. #S8032 |
| Guanosine 5’-diphosphate sodium type I (GDP) | Sigma-Aldrich | Cat. #G7127 |
| NuPAGE MES SDS Running Buffer (20X) | ThermoFisher Sci. | Cat. #NP000202 |
| NuPAGE Transfer Buffer (20X) | ThermoFisher Sci. | Cat. #NP0006-1 |
| NuPAGE LDS Sample Buffer | ThermoFisher Sci. | Cat. #NP0007 |
| Coomassie Brilliant Blue G-250 | Amresco | Cat. #0615 |
| Digitonin | Sigma-Aldrich | Cat. #D5628 |
| Native PAGE 20X Running buffer | ThermoFisher Sci. | Cat. #BN2001 |
| NuPAGE 4-12% Bis-Tris Protein Gels, 1.0 mm, 10-well | ThermoFisher Sci. | Cat. #NP0321 |
| NativePAGE 3-12% Bis-Tris Protein Gels, 1.0 mm, 15-well | ThermoFisher Sci. | Cat. #BN1003 |
| Protease inhibitor cocktail | Santa Cruz | Cat. #24948A |
| 5,5’-Dithiobis(2-nitrobenzoic acid) (DTNB) | Sigma-Aldrich | Cat. #D218200 |

| | | |
|---|---|---|
| Acetyl coenzyme A lithium salt | Sigma-Aldrich | Cat. #A2181 |
| Oxaloacetic acid | Sigma-Aldrich | Cat. #O4126 |
| Insulin from porcine pancreas | Sigma-Aldrich | Cat. #I5523 |
| Rosiglitazone Maleate | Sigma-Aldrich | Cat. #1605817 |
| BODIPY 558/568 C12 (4,4-Difluoro-5-(2-Thienyl)-4-Bora-3a,4a-Diaza-s-Indacene-3-Dodecanoic Acid) | ThermoFisher Sci. | Cat. #D3835 |
| Fatty Acid-Free Bovine Serum Albumin | EMD Millipore | Cat. #126575 |
| Collagenase Type II | Worthington | Cat. #E11231 |
| BODIPY 493/503 (4,4-Difluoro-1,3,5,7,8-Pentamethyl-4-Bora-3a,4a-Diaza-s-Indacene) | ThermoFisher Sci. | Cat. #D3922 |
| MitoTracker Deep Red FM | ThermoFisher Sci. | Cat. #M22426 |
| MitoTracker Green FM | ThermoFisher Sci. | Cat. #M7514 |
| Tetramethylrhodamine, Ethyl Ester, Perchlorate (TMRE) | ThermoFisher Sci. | Cat. #T669 |
| Ultrapure dimethyl sulfoxide (DMSO) | Amresco | Cat. #N182 |
| Sodium Pyruvate | ThermoFisher Sci. | Cat. #BP356 |
| DMEM | ThermoFisher Sci. | Cat. #31800022 |
| RPMI 1640 | ThermoFisher Sci. | Cat. #12100046 |
| Penicillin-Streptomycin | ThermoFisher Sci. | Cat. #15140 |
| Fetal calf serum | ThermoFisher Sci. | Cat. #16000 |
| Newborn calf serum | Sigma-Aldrich | Cat. #N4637 |
| STEMPro Accutase | ThermoFisher Sci. | Cat. #A1110501 |
| Critical Commercial Assays | | |
| Pierce BCA | ThermoFisher Sci. | Cat. #23225 |
| ECL Plus Western Blotting Substrate | ThermoFisher Sci. | Cat. #32132 |
| Free Glycerol Assay Kit | BioVision | Cat. #K630-100 |
| ATP Bioluminescence Assay Kit CLS II | Roche | Cat. #11699695001 |
| Experimental Models: Cell Lines | | |
| Pre-adipocytes | (Quirós et al., 2012) | N/A |
| INS1 832/13 | (Twig et al., 2008) | N/A |
| Software and Algorithms | | |
| ImageJ | NIH | https://fiji.sc/ |
| Graphpad | GraphPad Software | https://www.graphpad.com |
| Integrated Proteomics pipeline 2 | Integrated Proteomics Applications, Inc. | http://www.integratedproteomics.com/ |

# CHAPTER FOUR: Function and Physiology of Mitochondria Bound to Lipid Droplets


## Abstract

Mitochondria have been shown to associate with lipid droplets (LDs) in a variety of tissues and cell types but the functional role of these peridroplet mitochondria (PDM) remains is unknown. In this review we summarize the current evidence for the functional role of PDM in LD expansion and oxidation, the role of PDM in obesity pathophysiology, and the potential molecular mechanisms by which mitochondria are recruited to LDs. Much exciting experimental work remains to be done to unveil the physiological roles of PDM.


## Introduction

Cells require a continuous input of nutrients to maintain energy homeostasis. However, excess nutrients are harmful as fatty acids and glucose irreversibly modify proteins and disrupt cellular function. Cytoplasmic fatty acids imported from circulation or synthesized de novo are processed towards oxidative phosphorylation in the mitochondria or stored as triacylglycerides (TAGs) in lipid droplets (LDs) for later use. Free fatty acids destined for either oxidation or storage must first undergo ATP-dependent ligation to coenzyme A. Fatty acyl-CoAs destined for storage are sequentially esterified to glycerol backbone by glycerol-acyltransferases. On the other hand, fatty acyl-CoAs destined for oxidation are converted to acyl-carnitine on the outer mitochondrial membrane for mitochondrial import and oxidation. Mitochondria have been shown to physically contact lipid droplets in multiple tissues. It remains unclear whether PDM promote TAG synthesis,

fatty acid oxidation, or both. Here we review the current evidence on the structure and function of peridroplet mitochondria (PDM).

## What is the evidence for a role of PDM in LD expansion versus consumption?

Peridroplet mitochondria have been observed in a variety of cell culture models and tissue types. However, it remains unclear whether PDM promote lipid storage, oxidation, or both (Figure 4.1). To better understand the role of PDM, we have summarized the effect of different physiological conditions on the abundance of PDM, LD accumulation, and mitochondrial FAO (Table 4.1). If PDM play a role in LD accumulation, we expect that a higher proportion of mitochondria will be associated to LDs under physiological conditions of increased LD synthesis. On the other hand, if PDM is part of a cellular adaptation for fat oxidation, we expect PDM to increase in abundance under physiological conditions in which fatty acid oxidation rate is maximized.

*What can be learned about PDM from brown adipose tissue?*

Several groups have attempted to elucidate the role of PDM using brown adipose tissue (BAT), a system that robustly shifts from lipid storage to oxidation upon cold exposure (Cannon and Nedergaard 2004). Proteomic analysis by Yu et al. showed that 85 of the 130 measured mitochondrial proteins (65%) were undetectable or decreased in lipid droplets isolated from BAT of cold-exposed mice compared to mice housed in thermos-neutral conditions (Yu et al., 2015). This suggest that mitochondrial association to LDs is reduced under cold-exposure, when fatty acid oxidation is maximized for thermogenesis, compared to thermoneutral conditions, where fatty acids are primarily directed toward LD synthesis. Electron microscopy analysis of BAT isolated from thermoneutral and cold-adapted mice confirmed that mitochondrial depart from LDs upon

cold exposure (Benador et al., 2018). In addition, PDM isolated from BAT have been shown to have lower fatty acid oxidation capacity compared to cytoplasmic mitochondria (CM). These results support a role for PDM in BAT LD synthesis rather than oxidation.

*Do PDM play a role in LD expansion?*

Studies in cell culture models of LD expansion by oleate loading have observed a striking re-arrangement of mitochondria around LDs. Elegant work by Wang et al have shown that over expressing the lipid coat protein Perilipin5 (Plin5) uniquely recruits mitochondria to LDs (Wang et al. 2011) in addition to its regulation of adipose triacylglyceride lipase (ATGL). Over expression of Plin5, but not Plin1-4, resulted in complete mitochondrial recruitment to LDs and increased LD mass in CHO, AML12, HL-1 cells. This was later confirmed in vivo using transgenic Plin5 mice (H. Wang et al., 2013). However, since Plin5 over expression was only compared to GFP controls, it is not possible to discern from these studies if the changes in LD mass were a result of ATGL modulation or from mitochondrial recruitment to the LD surfaces. Later studies specifically determined the functional role of mitochondrial recruitment by comparing over expression of the full transcript of Plin5 to truncated Plin5 in which the C-terminal mitochondrial targeting sequence was specifically deleted (Benador et al. 2018). Experiments performed in both adipose and non-adipose cells confirmed that mitochondrial recruitment to the LDs doubled LD cross-sectional area and enhanced TAG synthesis independent of lipolysis regulation.

Remarkably, the TAG synthesizing enzyme diacylglycerol acyltransferase 2 (DGAT2) was also shown to recruit mitochondria to LDs in COS-7 cells. Stone et al. demonstrated that DGAT2 contains a unique mitochondrial targeting sequence that

recruits mitochondria to LDs upon stimulation of LD synthesis (Stone et al., 2009)(Figure 3). Over expression of DGAT2 resulted in complete mitochondrial recruitment to newly formed LDs and a doubling in size of LDs while over expression of DGAT1 or MGAT2, which do not contain a mitochondrial targeting sequence, did not recruit mitochondria to LDs nor increase LD size. These results thus support a role for mitochondrial recruitment in LD expansion in mammalian cell culture models of LD biogenesis induced by lipid loading.

PDM have also been observed in models of LD formation due to energy stress by multiple groups. Mouse embryonic fibroblasts deprived of nutrients showed a dramatic re-organization of mitochondria around lipid droplets and increased LD biogenesis. However, while Rambold et al. suggested these PDM direct the excess fatty acids liberated by autophagy toward mitochondrial beta oxidation, Nguyen et al. concluded that PDM direct fatty acid trafficking toward LD storage to protect mitochondria from lipotoxicity (Nguyen et al., 2017; Rambold et al., 2015). Thus, while LD expansion and mitochondrial recruitment are consistently observed in cell culture models of nutrient deprivation, it remains unclear whether PDM also play a role in fatty acid oxidation.

*Do PDM expand all LDs equally?*

The studies described above support a role of PDM in LD expansion. Importantly, the effects of mitochondrial recruitment on LD expansion in all studies centered on micro LDs (mLD, <2um), suggesting that mitochondrial recruitment may play a role in expansion of nascent LDs rather than expanding larger LDs. Indeed, mLDs appear to have the highest rates of TAG synthesis and expansion in cultured white adipocytes (Jude Deeney, personal communication). Furthermore, Zhang et al. demonstrated that mLDs have a

distinct lipid composition, protein composition, and organelle association in Huh7 cells, CHO K2 cells, mouse BAT, and mouse liver (Zhang et al., 2016). Indeed, studies have demonstrated that PDM enhance mLD expansion by providing ATP to power TAG synthesis, suggesting that PDM provide energy for ATP-dependent acyl-CoA synthesis (Benador et al. 2018). Consistent with this interpretation, Zhang et al. demonstrate that isolated mLD are capable of synthesizing TAGs in a cell-free environment when provided with ATP and CoA (Zhang et al., 2016). The exceptionally high $K_m$ value for ATP of Acyl CoA Synthetase (4.65mM) (Bar-Tana & Shapiro, 1975), suggest that ATP availability may be an important regulatory mechanism for TAG synthesis. Taken together, the studies reviewed above support the conclusion that PDM support mLD expansion by providing ATP for acyl-CoA synthesis in the TAG synthesis pathway. It remains an open question whether PDM further enhance TAG synthesis by additionally providing citrate for de novo lipogenesis.

**What is the biochemical nature of mitochondria-LD association and how is it regulated?**

The molecular composition and regulation of the bridge connecting mitochondria to LDs is currently unknown. However, several published reports have suggested potential models of the interaction (Table 2). Experiments with isolated organelles demonstrated that isolated mitochondria can interact with isolated LDs in a cell free environment (Jagerstrom et al.). This interaction was further enhanced by adding the cytoplasmic fraction, suggesting that factors both on the outer organellar membranes as well as in the cytoplasm promote mitochondria-LD interaction.

As mentioned above, work published by our and other labs have shown that the lipid droplet coat protein Perilipin 5 (Plin5), but not Plin1-4, strongly recruits mitochondria to the LDs in CHO, AML12, HL-1 cells, primary brown adipocytes, and INS1 cells, and mouse heart. Site-directed mutagenesis unveiled a highly conserved sequence of the C-terminus that recruits mitochondria to LDs. Additional experiments show that fusing Plin2, which induces LD formation but does not recruit mitochondria on its own, to the C-terminus of Plin5 is sufficient to induce mitochondrial recruitment. However, despite considerable efforts to elucidate the protein or membrane partner of Plin5, the molecular mechanism by which Plin5 recruits mitochondria remains unclear (Carole Sztalyrd, personal communication). Interestingly, a recent report by Gallardo-Montejano et al. demonstrated that phosphorylated Plin5 translocated to the nucleus, where it partners with PGC1alpha to regulate gene transcription (Gallardo-Montejano et al., 2016). This suggests that Plin5 may regulate mitochondrial recruitment to LDs indirectly through signaling pathways rather than direct biochemical interaction.

Additional protein candidates have been suggested. Stone et al. showed that diacylglycerol acyltransferase 2 (DGAT2), which is known to localize to ER and LDs membranes, also possess an N-terminal mitochondrial targeting sequence using site-directed mutagenesis. Additional experiments demonstrated that fusing the N-terminus to RFP was sufficient to target it to mitochondria. These data suggest that DGAT2 directly interacts with both LD and mitochondrial membranes.

Protein-protein interaction as a mechanism of mitochondria-LD association has previously been suggested (Boutant et al., 2017). However, elegant biochemical experiments in isolated BAT LDs demonstrated that mitochondrial association to LDs is resistant to tryptic

digestion and high salt wash that disrupt protein-protein interactions (Yu et al., 2015). The sensitivity of mitochondria-LD association to detergent wash suggested that, while protein-protein interaction may be involved in initiation of mitochondrial requirement, mitochondria-LD association it is ultimately stabilized by additional membrane-protein and/or membrane-membrane interactions, such as hemifusion. This interpretation is supported by the increased thickness and enhanced electron density of membranes observed in the interface of mitochondria-LD association by electron microscopy studies (Benador et al., 2018).

## What is the role of PDM in obesity?

Obesity is characterized by hypertrophic and hyperplastic adipose tissue hypertrophy and intracellular lipid accumulation in liver and muscle. Whether PDM play a role in lipid accumulation in obesity remains an open question. We summarize the current evidence for the involvement of PDM in obesity-related lipid droplet accumulation below.

*Do PDM play a role in adipose tissue expansion?*

Hyperplastic and hypertrophic WAT hypertrophy are the hallmarks of obesity. Studies have consistently shown that white adipocytes in early stages of differentiation, when LD synthesis is highest, have high levels of mitochondrial mass compared to adipocytes late stages of differentiation, where LD synthesis is relatively low. While there is currently no direct evidence for the existence of PDM in WAT, the association between mitochondrial mass and LD synthesis rate suggests a potential role for PDM in LD building in the early stages of adipocyte differentiation. Indeed, our unpublished microscopic observations confirmed that cultured white adipocytes have high levels of PDM in early stages of differentiation, where LD synthesis is maximal. In conclusion, there is currently

no direct published evidence for the existence of PDM in WAT but our unpublished observations suggest that PDM may play in hyperplastic adipose tissue growth. This will need to be confirmed by future studies.

*Do PDM play a role in intramyocellular lipid accumulation?*

Muscle tissue synthesizes lipid droplets under multiple metabolic conditions, including fasting, endurance training, and over feeding. In heart, Wang et al. have demonstrated that fasted mice have increased levels of PDM in addition to increased LD accumulation (H. Wang et al., 2013). Transgenic mice over expressing Plin5 had enhanced cardiac LD accumulation under both fed and fasted conditions as well as a reduction in lipid utilization. On the other hand, whole body Plin5KO mice had severe cardiac LD depletion, increased fatty acid oxidation, and ROS-mediated cardiac dysfunction (Kuramoto et al., 2012). However, the recovery of LDs in animals treated with lipase inhibitors suggests that lipolysis dysregulation in Plin5KO animals played a significant role in this phenotype. Taken together, these studies suggest that PDM could play a role in cardiac LD accumulation but further studies are needed to precisely define their physiology.

In skeletal muscle, LDs have been shown to accumulate both obese and trained athletes with opposite effects on insulin sensitivity (athlete's paradox). Electron microscopy evidence has demonstrated that endurance exercise increased levels of PDM and LD accumulation in human skeletal muscle (Tarnopolsky et al., 2007). Remarkably, the subcellular location of LDs in trained individuals was interfibrillar compared to subsarcolemmal in obese individuals (Nielsen et al. 2017). Since PDM appear to localize to interfibrillar region of muscle fibers, we may infer from these studies that PDM play a

role in adaptive rather than pathological LD accumulation. Indirect evidence in support of this suggestion is that muscle-specific Plin5 over expression increased PDM (Bosma et al., 2012) and protected muscle tissue from high fat diet-induced lipotoxicity (Laurens et al., 2016). However, as mentioned before, it remains unclear whether Plin5 effects are mediated by lipolysis regulatory function, mitochondrial recruitment, or both. In summary, additional studies are needed to determine the precise role of PDM in physiological and pathological LD accumulation in muscle tissue.

*What is the evidence that PDM exist in liver?*

The liver is specialized to synthesize lipids post-prandially for distribution to other tissues. In pathological conditions, the liver accumulates excess lipid droplets, which eventually progress to a chronic inflammatory state and cirrhosis. Although PDM have not been specifically studied and quantified in liver, various evidence suggest that PDM may exist and play a role in hepatocytes. For example, published electron microscopy images of livers from HFD and genetic models of obesity appear to have increases levels of PDM (Arruda et al., 2014)(Figure 1, Supplemental Figure 1). Furthermore, high-fat feeding has been shown to increase Plin5 expression in both human and mouse liver tissue (C. Wang et al., 2015) and the over expression of Plin5 (Trevino et al., 2015) and DGAT2 (Monetti et al., 2007) increased LD mass and protected against lipotoxic liver injury. In summary, there is currently no direct evidence for the existence or physiological relevance of PDM in liver tissue and additional studies are warranted.

## What is the physiological role of LDs synthesized by PDM?

Determining the role of PDM requires gain-of-function and loss-of-function models that are currently lacking. An experimental system where mitochondrial association to LDs

can be acutely disrupted would be ideal to determine its physiological significance. While this system has yet to be developed, several genetic models have been reported in which mitochondria-LD association was found to be reduced.

Our lab has recently published on a mouse model that serendipitously had a reduction in PDM (Mahdaviani et al., 2017). Mice with BAT-specific knock out of the mitochondrial fusion protein Mfn2 had severely diminished mitochondrial association with LDs. Interestingly, Mfn2KO BAT had enhanced mitochondrial fatty acid oxidation capacity concomitant with increased LD synthesis. One interpretation of these results is that Mfn2KO BAT has enhanced capacity to oxidize fatty acids coming from circulation but reduced capacity to oxidize fatty acids from LDs. This phenotype is reminiscent of muscular tissue from obese individuals, where Mfn2 is downregulated and dysfunctional LD content is increased. These findings suggest that the macro LDs accumulated in the absence of Mfn2 and PDM represent a functionally different class than mLDs synthesized in the presence of PDM. This interpretation is consistent with reports functional heterogeneity of LDs from different size classes (Zhang et al., 2016). The severe BAT dysfunction and cold-intolerance exhibited by Mfn2KO mice leads us to speculate that mLDs synthesized in the presence of PDM may represent a compartmentalized pool of TAGs destined for oxidation as opposed to the macro LDs that are inaccessible during cold exposure. This view is consistent with the work from Rosalind Coleman's group that demonstrated the existence of compartmentalized metabolic pools of fatty acid metabolites (Cooper, Young, Klett, & Coleman, 2015; Ellis et al., 2010; L. O. Li et al., 2015). Future work will be needed to confirm if and how PDM synthesize a compartmentalized lipid pool.

## Conclusions

This is an exciting time for PDM research. Work reported in the last decade has opened a new territory of cell biology that may have important implications for fat metabolism. However, animal models that specifically disrupt mitochondria-LD interaction are still needed to better understand the physiological impact of this phenomenon. A better understanding PDM and LD biology is of great importance as the twin pandemics of obesity and type 2 diabetes mellitus continue to soar and decrease lifespan and healthspan. We hope that this research avenue will bear new insights into cell metabolism and ultimately translate to more effective therapies for obesity and type 2 diabetes.

## Figures

**Figure 4.1. Illustrations of the potential roles of peridroplet mitochondria.**

Peridropet mitochondria consume lipid droplet

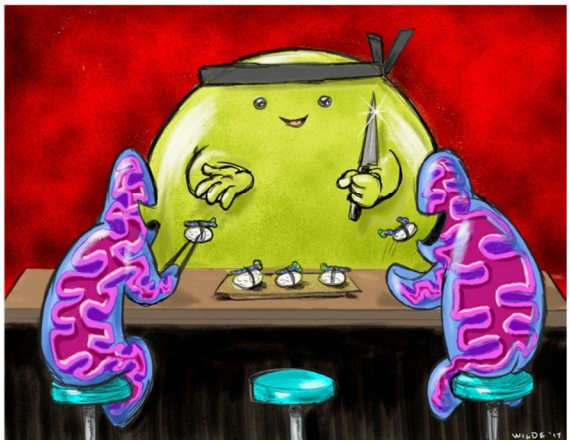

Peridroplet mitochondria expand lipid droplet

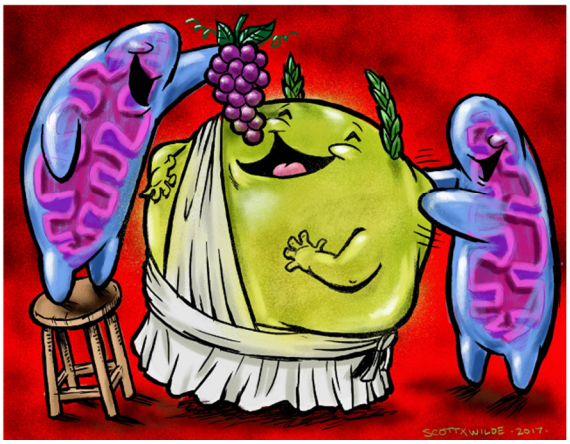

## Tables

| **Table 4.1. Conditions that increase mitochondrial recruitment to LDs** | | | | | |
|---|---|---|---|---|---|
| | Cell type | Condition | Mito-LD interaction | LD Mass | FAO |
| *Brown adipose tissue* | | | | | |
| (Benador et al., 2018) | Mouse BAT | Thermoneutrality compared to cold exposure | Higher | Higher | Lower |
| (Yu et al., 2015) | Mouse BAT | Thermoneutrality compared to cold exposure | Higher (Table S6) | Higher | Lower |
| *Cell culture* | | | | | |
| (H. Wang et al., 2011) | CHO, AML12, HL-1 cells | Oleate loading in Plin5 over expression vs GFP control | Higher | Higher | Lower |
| (Benador et al., 2018) | Primary brown adipocytes | Plin5 vs C-truncated Plin5 | Higher | Higher | N/A |
| (Stone et al., 2009) | COS-7 | Oleate loading DGAT2 over expression vs DGAT1 and MGAT2 | Higher | Higher | N/A |
| (Rambold et al., 2015) | MEF | Nutrient deprivation compared to complete medium | Higher | Higher | Higher |
| (Nguyen et al., 2017, p. 1) | MEF | Nutrient deprivation compared to complete medium | Higher | Higher | Higher |
| *Striated muscle* | | | | | |
| (Tarnopolsky et al., 2007) | Human Vastus Lateralis muscle | Post-endurance training vs pre-training | Higher | Higher | Higher |
| (H. Wang et al., 2013) | Mouse Heart | Plin5 over expression vs Wild Type | Higher | Higher | Lower |
| (H. Wang et al., 2013) | Mouse Heart | Fasting vs feeding | Higher | Higher | Lower |
| *Liver* | | | | | |
| (Arruda et al., 2014) | Mouse liver | Ob/Ob vs wt<br>HFD vs chow | Higher | Higher | N/A |

**Table 4.2. Hypothesized mediators and regulators of Mitochondria-LD interaction**

| | Cell type | Technique | Potential mediators of mitochondria-LD association |
|---|---|---|---|
| (Jägerström et al., 2009) | NIH 3T3 | Isolated mitochondria and lipid droplets in a cell-free system | Factors on outer surfaces of organelles and factors in cytoplasmic fraction. |
| (H. Wang et al., 2011)<br>Benador et al. 2018 | CHO, AML12, HL-1<br>Primary brown adipocytes, INS1 | Site-directed mutagenesis and confocal fluorescence microscopy. | C-terminus of Plin5 as potential regulator (Mitochondrial target unknown) |
| (Stone et al., 2009) | COS-7 | Site-directed mutagenesis, confocal fluorescence microscopy, and cell fractionation. | N-terminus of DGAT2 as potential recruiter (Directly targets outer mitochondrial membrane) |
| (Boutant et al., 2017) | Primary brown adipocytes | Co-IP | Plin1-Mfn2 |
| (Yu et al., 2015) | BAT | Western blot analysis of mitochondrial proteins in isolated lipid droplets subjected to tryptic digestion, high salt wash, and detergent wash. | Membrane hemifusion (Also supported by membrane thickening observed by EM) |

## BIBLIOGRAPHY

Anand, R., Wai, T., Baker, M. J., Kladt, N., Schauss, A. C., Rugarli, E., & Langer, T. (2014). The i-AAA protease YME1L and OMA1 cleave OPA1 to balance mitochondrial fusion and fission. *The Journal of Cell Biology*, *204*(6), 919–929. https://doi.org/10.1083/jcb.201308006

Arruda, A. P., Pers, B. M., Parlakgül, G., Güney, E., Inouye, K., & Hotamisligil, G. S. (2014). Chronic enrichment of hepatic endoplasmic reticulum-mitochondria contact leads to mitochondrial dysfunction in obesity. *Nature Medicine*, *20*(12), 1427–1435. https://doi.org/10.1038/nm.3735

Bar-Tana, J., & Shapiro, B. (1975). Long-chain fatty acyl-CoA synthetase from rat liver microsomes. EC 6.2.1.3 fatty acyl-CoA ligase (ATP). *Methods in Enzymology*, *35*, 117–122.

Benador, I. Y., Veliova, M., Mahdaviani, K., Petcherski, A., Wikstrom, J. D., Assali, E., … Shirihai, O. S. (2018). Mitochondria Bound to Lipid Droplets Have Unique Bioenergetics, Composition, and Dynamics That Support Lipid Droplet Expansion. *Cell Metabolism*, *27*(4), 869–885. https://doi.org/10.1016/j.cmet.2018.03.003

Bosma, M., Minnaard, R., Sparks, L. M., Schaart, G., Losen, M., de Baets, M. H., … Hesselink, M. K. C. (2012). The lipid droplet coat protein perilipin 5 also localizes to muscle mitochondria. *Histochemistry and Cell Biology*, *137*(2), 205–216. https://doi.org/10.1007/s00418-011-0888-x

Boss, O., & Farmer, S. R. (2012). Recruitment of brown adipose tissue as a therapy for obesity-associated diseases. *Frontiers in Endocrinology*, *3*, 1–6. https://doi.org/10.3389/fendo.2012.00014

Boutant, M., Kulkarni, S. S., Joffraud, M., Ratajczak, J., Valera-Alberni, M., Combe, R., … Cantó, C. (2017). Mfn2 is critical for brown adipose tissue thermogenic function. *The EMBO Journal*, *36*(11), 1543–1558. https://doi.org/10.15252/embj.201694914

Calvo, S. E., Clauser, K. R., & Mootha, V. K. (2016). MitoCarta2.0: an updated inventory of mammalian mitochondrial proteins. *Nucleic Acids Research*, *44*(D1), D1251-1257. https://doi.org/10.1093/nar/gkv1003

Cannon, B., & Nedergaard, J. (2001). Respiratory and thermogenic capacities of cells and mitochondria from brown and white adipose tissue. *Methods in Molecular Biology (Clifton, N.J.)*, *155*, 295–303. https://doi.org/10.1385/1-59259-231-7:295

Cannon, B., & Vogel, G. (1977). The mitochondrial ATPase of brown adipose tissue. Purification and comparison with the mitochondrial ATPase from beef heart. *FEBS Letters*, *76*(2), 284–289.

Cannon, Barbara, & Nedergaard, J. (2004). Brown adipose tissue: function and physiological significance. *Physiological Reviews*, *84*(1), 277–359. https://doi.org/10.1152/physrev.00015.2003

Cereghetti, G. M., Stangherlin, A., de Brito, O. M., Chang, C. R., Blackstone, C., Bernardi, P., & Scorrano, L. (2008). Dephosphorylation by calcineurin regulates translocation of Drp1 to mitochondria. *Proceedings of the National Academy of Sciences of the United States of America*, *105*(41), 15803–15808. https://doi.org/10.1073/pnas.0808249105

Chen, H., Chomyn, A., & Chan, D. C. (2005). Disruption of Fusion Results in Mitochondrial Heterogeneity and Dysfunction. *Journal of Biological Chemistry*, *280*(28), 26185–26192. https://doi.org/10.1074/jbc.M503062200

Chen, H., Detmer, S. A., Ewald, A. J., Griffin, E. E., Fraser, S. E., & Chan, D. C. (2003). Mitofusins Mfn1 and Mfn2 coordinately regulate mitochondrial fusion and are essential for embryonic development. *The Journal of Cell Biology*, *160*(2), 189–200. https://doi.org/10.1083/jcb.200211046

Cinti, S., Cancello, R., Zingaretti, M. C., Ceresi, E., De Matteis, R., Giordano, A., … Ricquier, D. (2002). CL316,243 and cold stress induce heterogeneous expression of UCP1 mRNA and protein in rodent brown adipocytes. *The Journal of Histochemistry and Cytochemistry: Official Journal of the*

*Histochemistry Society*, *50*(1), 21–31. https://doi.org/10.1177/002215540205000103

Cooper, D. E., Young, P. A., Klett, E. L., & Coleman, R. A. (2015). Physiological Consequences of Compartmentalized Acyl-CoA Metabolism. *The Journal of Biological Chemistry*, *290*(33), 20023–20031. https://doi.org/10.1074/jbc.R115.663260

Cottet-Rousselle, C., Ronot, X., Leverve, X., & Mayol, J.-F. (2011). Cytometric assessment of mitochondria using fluorescent probes. *Cytometry. Part A: The Journal of the International Society for Analytical Cytology*, *79*(6), 405–425. https://doi.org/10.1002/cyto.a.21061

Ding, Y., Zhang, S., Yang, L., Na, H., Zhang, P., Zhang, H., … Liu, P. (2013). Isolating lipid droplets from multiple species. *Nature Protocols*, *8*(1), 43–51. https://doi.org/10.1038/nprot.2012.142

Divakaruni, A. S., Rogers, G. W., & Murphy, A. N. (2014). Measuring Mitochondrial Function in Permeabilized Cells Using the Seahorse XF Analyzer or a Clark-Type Oxygen Electrode. *Current Protocols in Toxicology*, *60*, 25.2.1-16. https://doi.org/10.1002/0471140856.tx2502s60

Djafarzadeh, S., & Jakob, S. M. (2017). Isolation of Intact Mitochondria from Skeletal Muscle by Differential Centrifugation for High-resolution Respirometry Measurements. *Journal of Visualized Experiments: JoVE*, (121). https://doi.org/10.3791/55251

Eaton, S. (2002). Control of mitochondrial beta-oxidation flux. *Progress in Lipid Research*, *41*(3), 197–239.

Ellis, J. M., Li, L. O., Wu, P.-C., Koves, T. R., Ilkayeva, O., Stevens, R. D., … Coleman, R. A. (2010). Adipose acyl-CoA synthetase-1 (ACSL1) directs fatty acids towards β-oxidation and is required for cold thermogenesis. *Cell Metabolism*, *12*(1), 53–64. https://doi.org/10.1016/j.cmet.2010.05.012

Farese, R. V., & Walther, T. C. (2009). Lipid Droplets Finally Get a Little R-E-S-P-E-C-T. *Cell*, *139*, 855–860.

Fasshauer, M., Klein, J., Ueki, K., Kriauciunas, K. M., Benito, M., White, M. F., & Kahn, C. R. (2000). Essential role of insulin receptor substrate-2 in insulin stimulation of Glut4 translocation and glucose uptake in brown adipocytes. *The Journal of Biological Chemistry*, *275*(33), 25494–25501. https://doi.org/10.1074/jbc.M004046200

Fedorenko, A., Lishko, P. V., & Kirichok, Y. (2012). Mechanism of fatty-acid-dependent UCP1 uncoupling in brown fat mitochondria. *Cell*, *151*(2), 400–413. https://doi.org/10.1016/j.cell.2012.09.010

Forner, F., Kumar, C., Luber, C. A., Fromme, T., Klingenspor, M., & Mann, M. (2009). Proteome differences between brown and white fat mitochondria reveal specialized metabolic functions. *Cell Metabolism*, *10*(4), 324–335. https://doi.org/10.1016/j.cmet.2009.08.014

Gallardo-Montejano, V. I., Saxena, G., Kusminski, C. M., Yang, C., McAfee, J. L., Hahner, L., … Bickel, P. E. (2016). Nuclear Perilipin 5 integrates lipid droplet lipolysis with PGC-1α/SIRT1-dependent transcriptional regulation of mitochondrial function. *Nature Communications*, *7*, 12723. https://doi.org/10.1038/ncomms12723

Garland, P. B., Shepherd, D., Nicholls, D. G., & Ontko, J. (1968). Energy-dependent control of the tricarboxylic acid cycle by fatty acid oxidation in rat liver mitochondria. *Advances in Enzyme Regulation*, *6*, 3–30.

Huff, J., Bathe, W., Netz, R., Anhut, T., & Weisshart, K. (2015, July). The Airyscan Detector from ZEISS Confocal Imaging with Improved Signal-to-Noise Ratio and Superresolution. Carl Zeiss Microscopy GmbH, Germany. Retrieved from https://applications.zeiss.com/C125792900358A3F/0/BF16BECDC08849E1C1257ED60029AF8D/$FILE/EN_41_013_105_wp_Airyscan-detector.pdf

Jägerström, S., Polesie, S., Wickström, Y., Johansson, B. R., Schröder, H. D., Højlund, K., & Boström, P. (2009). Lipid droplets interact with mitochondria

using SNAP23. *Cell Biology International*, *33*(9), 934–940. https://doi.org/10.1016/j.cellbi.2009.06.011

Klop, B., Elte, J. W. F., & Cabezas, M. C. (2013). Dyslipidemia in Obesity: Mechanisms and Potential Targets. *Nutrients*, *5*, 1218–1240.

Kuramoto, K., Okamura, T., Yamaguchi, T., Nakamura, T. Y., Wakabayashi, S., Morinaga, H., … Osumi, T. (2012). Perilipin 5, a lipid droplet-binding protein, protects heart from oxidative burden by sequestering fatty acid from excessive oxidation. *The Journal of Biological Chemistry*, *287*(28), 23852–23863. https://doi.org/10.1074/jbc.M111.328708

Langousis, G., Shimogawa, M. M., Saada, E. A., Vashisht, A. A., Spreafico, R., Nager, A. R., … Hill, K. L. (2016). Loss of the BBSome perturbs endocytic trafficking and disrupts virulence of Trypanosoma brucei. *Proceedings of the National Academy of Sciences*, *113*(3), 632–637. https://doi.org/10.1073/pnas.1518079113

Lapuente-Brun, E., Moreno-Loshuertos, R., Acín-Pérez, R., Latorre-Pellicer, A., Colás, C., Balsa, E., … Enríquez, J. A. (2013). Supercomplex assembly determines electron flux in the mitochondrial electron transport chain. *Science (New York, N.Y.)*, *340*(6140), 1567–1570. https://doi.org/10.1126/science.1230381

Laurens, C., Bourlier, V., Mairal, A., Louche, K., Badin, P.-M., Mouisel, E., … Moro, C. (2016). Perilipin 5 fine-tunes lipid oxidation to metabolic demand and protects against lipotoxicity in skeletal muscle. *Scientific Reports*, *6*, 38310. https://doi.org/10.1038/srep38310

Li, L. O., Grevengoed, T. J., Paul, D. S., Ilkayeva, O., Koves, T. R., Pascual, F., … Coleman, R. A. (2015). Compartmentalized acyl-CoA metabolism in skeletal muscle regulates systemic glucose homeostasis. *Diabetes*, *64*(1), 23–35. https://doi.org/10.2337/db13-1070

Li, Y., Fromme, T., Schweizer, S., Schöttl, T., & Klingenspor, M. (2014). Taking control over intracellular fatty acid levels is essential for the analysis of thermogenic function in cultured primary brown and brite/beige

adipocytes. *EMBO Reports*, *15*(10), 1069–1076. https://doi.org/10.15252/embr.201438775

Liesa, M., & Shirihai, O. S. (2013). Mitochondrial dynamics in the regulation of nutrient utilization and energy expenditure. *Cell Metabolism*, *17*(4), 491–506. https://doi.org/10.1016/j.cmet.2013.03.002

Lindberg, O., de Pierre, J., Rylander, E., & Afzelius, B. A. (1967). Studies of the mitochondrial energy-transfer system of brown adipose tissue. *The Journal of Cell Biology*, *34*(1), 293–310.

Mahdaviani, K., Benador, I. Y., Su, S., Gharakhanian, R. A., Stiles, L., Trudeau, K. M., … Shirihai, O. S. (2017). Mfn2 deletion in brown adipose tissue protects from insulin resistance and impairs thermogenesis. *EMBO Reports*. https://doi.org/10.15252/embr.201643827

Mashek, D. G., Li, L. O., & Coleman, R. A. (2007). Long-chain acyl-CoA synthetases and fatty acid channeling. *Future Lipidology*, *2*(4), 465–476.

Mitchell, N., Catenacci, V., Wyatt, H. R., & Hill, J. O. (2018). Obesity: overview of an epidemic. *Psychiatric Clinics of North America*, *34*, 717–732.

Monetti, M., Levin, M. C., Watt, M. J., Sajan, M. P., Marmor, S., Hubbard, B. K., … Farese, R. V. (2007). Dissociation of hepatic steatosis and insulin resistance in mice overexpressing DGAT in the liver. *Cell Metabolism*, *6*(1), 69–78. https://doi.org/10.1016/j.cmet.2007.05.005

Nakada, K., Inoue, K., Ono, T., Isobe, K., Ogura, A., Goto, Y. I., … Hayashi, J. I. (2001). Inter-mitochondrial complementation: Mitochondria-specific system preventing mice from expression of disease phenotypes by mutant mtDNA. *Nature Medicine*, *7*(8), 934–940. https://doi.org/10.1038/90976

Nguyen, T. B., Louie, S. M., Daniele, J. R., Tran, Q., Dillin, A., Zoncu, R., … Olzmann, J. A. (2017). DGAT1-Dependent Lipid Droplet Biogenesis Protects Mitochondrial Function during Starvation-Induced Autophagy.

*Developmental Cell*, *42*(1), 9–21.e5. https://doi.org/10.1016/j.devcel.2017.06.003

Palmer, J. W., Tandler, B., & Hoppel, C. L. (1977). Biochemical properties of subsarcolemmal and interfibrillar mitochondria isolated from rat cardiac muscle. *The Journal of Biological Chemistry*, *252*(23), 8731–8739.

Prentki, M., & Madiraju, S. R. M. (2012). Glycerolipid/free fatty acid cycle and islet β-cell function in health, obesity and diabetes. *Molecular and Cellular Endocrinology*, *353*(1–2), 88–100. https://doi.org/10.1016/j.mce.2011.11.004

Quirós, P. M., Ramsay, A. J., Sala, D., Fernández-Vizarra, E., Rodríguez, F., Peinado, J. R., … López-Otín, C. (2012). Loss of mitochondrial protease OMA1 alters processing of the GTPase OPA1 and causes obesity and defective thermogenesis in mice. *The EMBO Journal*, *31*(9), 2117–2133. https://doi.org/10.1038/emboj.2012.70

Rambold, A. S., Cohen, S., & Lippincott-Schwartz, J. (2015). Fatty acid trafficking in starved cells: regulation by lipid droplet lipolysis, autophagy, and mitochondrial fusion dynamics. *Developmental Cell*, *32*(6), 678–692. https://doi.org/10.1016/j.devcel.2015.01.029

Rogers, G. W., Brand, M. D., Petrosyan, S., Ashok, D., Elorza, A. A., Ferrick, D. A., & Murphy, A. N. (2011). High Throughput Microplate Respiratory Measurements Using Minimal Quantities Of Isolated Mitochondria. *PLOS ONE*, *6*(7), e21746. https://doi.org/10.1371/journal.pone.0021746

Rosca, M. G., Vazquez, E. J., Kerner, J., Parland, W., Chandler, M. P., Stanley, W., … Hoppel, C. L. (2008). Cardiac mitochondria in heart failure: decrease in respirasomes and oxidative phosphorylation. *Cardiovascular Research*, *80*(1), 30–39. https://doi.org/10.1093/cvr/cvn184

Smirnova, E., Griparic, L., Shurland, D. L., & van der Bliek, A. M. (2001). Dynamin-related protein Drp1 is required for mitochondrial division in mammalian cells. *Molecular Biology of the Cell*, *12*(8), 2245–2256.

Spinazzi, M., Casarin, A., Pertegato, V., Salviati, L., & Angelini, C. (2012). Assessment of mitochondrial respiratory chain enzymatic activities on tissues and cultured cells. *Nature Protocols*, *7*(6), 1235–1246. https://doi.org/10.1038/nprot.2012.058

Stone, S. J., Levin, M. C., Zhou, P., Han, J., Walther, T. C., & Farese, R. V. (2009). The endoplasmic reticulum enzyme DGAT2 is found in mitochondria-associated membranes and has a mitochondrial targeting signal that promotes its association with mitochondria. *The Journal of Biological Chemistry*, *284*(8), 5352–5361. https://doi.org/10.1074/jbc.M805768200

Tarnopolsky, M. A., Rennie, C. D., Robertshaw, H. A., Fedak-Tarnopolsky, S. N., Devries, M. C., & Hamadeh, M. J. (2007). Influence of endurance exercise training and sex on intramyocellular lipid and mitochondrial ultrastructure, substrate use, and mitochondrial enzyme activity. *American Journal of Physiology. Regulatory, Integrative and Comparative Physiology*, *292*(3), R1271-1278. https://doi.org/10.1152/ajpregu.00472.2006

Trevino, M. B., Mazur-Hart, D., Machida, Y., King, T., Nadler, J., Galkina, E. V., … Imai, Y. (2015). Liver Perilipin 5 Expression Worsens Hepatosteatosis But Not Insulin Resistance in High Fat-Fed Mice. *Molecular Endocrinology (Baltimore, Md.)*, *29*(10), 1414–1425. https://doi.org/10.1210/me.2015-1069

Twig, G., Elorza, A., Molina, A. J. A., Mohamed, H., Wikstrom, J. D., Walzer, G., … Shirihai, O. S. (2008). Fission and selective fusion govern mitochondrial segregation and elimination by autophagy. *The EMBO Journal*, *27*(2), 433–446. https://doi.org/10.1038/sj.emboj.7601963

Twig, G., Liu, X., Liesa, M., Wikstrom, J. D., Molina, A. J. A., Las, G., … Shirihai, O. S. (2010). Biophysical properties of mitochondrial fusion events in pancreatic β-cells and cardiac cells unravel potential control mechanisms of its selectivity. *American Journal of Physiology - Cell Physiology*, *299*(2), C477–C487. https://doi.org/10.1152/ajpcell.00427.2009

Wang, C., Zhao, Y., Gao, X., Li, L., Yuan, Y., Liu, F., … Ye, J. (2015). Perilipin 5 improves hepatic lipotoxicity by inhibiting lipolysis. *Hepatology (Baltimore, Md.)*, *61*(3), 870–882. https://doi.org/10.1002/hep.27409

Wang, H., Sreenivasan, U., Gong, D.-W., O'Connell, K. A., Dabkowski, E. R., Hecker, P. A., … Sztalryd, C. (2013). Cardiomyocyte-specific perilipin 5 overexpression leads to myocardial steatosis and modest cardiac dysfunction1. *Journal of Lipid Research*, *54*(4), 953–965. https://doi.org/10.1194/jlr.M032466

Wang, H., Sreenivasan, U., Sreenevasan, U., Hu, H., Saladino, A., Polster, B. M., … Sztalryd, C. (2011). Perilipin 5, a lipid droplet-associated protein, provides physical and metabolic linkage to mitochondria. *Journal of Lipid Research*, *52*(12), 2159–2168. https://doi.org/10.1194/jlr.M017939

Wibom, R., Lundin, A., & Hultman, E. (1990). A sensitive method for measuring ATP-formation in rat muscle mitochondria. *Scandinavian Journal of Clinical and Laboratory Investigation*, *50*(2), 143–152.

Wikstrom, J. D., Mahdaviani, K., Liesa, M., Sereda, S. B., Si, Y., Las, G., … Shirihai, O. S. (2014). Hormone-induced mitochondrial fission is utilized by brown adipocytes as an amplification pathway for energy expenditure. *The EMBO Journal*, *33*(5), 418–436. https://doi.org/10.1002/embj.201385014

Wikstrom, J. D., Twig, G., & Shirihai, O. S. (2009). What can mitochondrial heterogeneity tell us about mitochondrial dynamics and autophagy? *The International Journal of Biochemistry & Cell Biology*, *41*(10), 1914–1927. https://doi.org/10.1016/j.biocel.2009.06.006

Wittig, I., Braun, H.-P., & Schägger, H. (2006). Blue native PAGE. *Nature Protocols*, *1*(1), 418–428. https://doi.org/10.1038/nprot.2006.62

Yu, J., Zhang, S., Cui, L., Wang, W., Na, H., Zhu, X., … Liu, P. (2015). Lipid droplet remodeling and interaction with mitochondria in mouse brown adipose tissue during cold treatment. *Biochimica Et Biophysica Acta*, *1853*(5), 918–928. https://doi.org/10.1016/j.bbamcr.2015.01.020

Zechner, R., Zimmermann, R., Elchmann, T. O., Kohlwein, S. D., Haemmerle, G., Lass, A., & Madeo, F. (2012). FAT SIGNALS - Lipases and Lipolysis in Lipid Metabolism and Signaling. *Cell Metabolism*, *15*, 279–291.

Zhang, S., Wang, Y., Cui, L., Deng, Y., Xu, S., Yu, J., … Liu, P. (2016). Morphologically and Functionally Distinct Lipid Droplet Subpopulations. *Scientific Reports*, *6*, 29539. https://doi.org/10.1038/srep29539

## CURRICULUM VITAE